Extragalactic Magnetism with SOFIA (SALSA Legacy Program). V. First Results on the Magnetic Field Orientation of Galaxies

Alejandro S. Borlaff[1,2,3] , Enrique Lopez-Rodriguez[3] , Rainer Beck[4], Susan E. Clark[3,5] , Evangelia Ntormousi[6,7] ,
Konstantinos Tassis[7,8] , Sergio Martin-Alvarez[3], Mehrnoosh Tahani[3] , Daniel A. Dale[9] , Ignacio del Moral-Castro[10,11] ,
Julia Roman-Duval[12] , Pamela M. Marcum[1], John E. Beckman[11,13] , Kandaswamy Subramanian[14,15],
Sarah Eftekharzadeh[16] , and Leslie Proudfit[17]

[1] NASA Ames Research Center, Moffett Field, CA 94035, USA; a.s.borlaff@nasa.gov
[2] Bay Area Environmental Research Institute, Moffett Field, CA 94035, USA
[3] Kavli Institute for Particle Astrophysics & Cosmology (KIPAC), Stanford University, Stanford, CA 94305, USA
[4] Max-Planck-Institut für Radioastronomie, Auf dem Hügel 69, D-53121 Bonn, Germany
[5] Department of Physics, Stanford University, Stanford, CA 94305, USA
[6] Scuola Normale Superiore di Pisa, Piazza dei Cavalieri 7, Pisa, Italy
[7] Institute of Astrophysics, Foundation for Research and Technology-Hellas, Vasilika Vouton, GR-70013 Heraklion, Greece
[8] Department of Physics & ITCP, University of Crete, GR-70013, Heraklion, Greece
[9] Department of Physics and Astronomy, University of Wyoming, Laramie, WY 82071, USA
[10] Kapteyn Astronomical Institute, University of Groningen, P.O. Box 800, 9700 AV Groningen, The Netherlands
[11] Facultad de Física, Universidad de La Laguna, Avda. Astrofísico Fco. Sánchez s/n, E-38200, La Laguna, Tenerife, Spain
[12] Space Telescope Science Institute, 3700 San Martin Drive, Baltimore, MD 21218, USA
[13] Instituto de Astrofísica de Canarias, C/ Vía Láctea, E-38200 La Laguna, Tenerife, Spain
[14] IUCAA, Post Bag 4, Ganeshkhind, Pune 411007, India
[15] Department of Physics, Ashoka University, Rajiv Gandhi Education City, Rai, Sonipat 131029, Haryana, India
[16] NASA Goddard Space Flight Center, 8800 Greenbelt Road, Greenbelt, MD 20771, USA
[17] SOFIA Science Center, NASA Ames Research Center, Moffett Field, CA 94035, USA

Abstract

We present the analysis of the magnetic field (B-field) structure of galaxies measured with far-infrared (FIR) and radio (3 and 6 cm) polarimetric observations. We use the first data release of the Survey of extragALactic magnetiSm with SOFIA of 14 nearby (<20 Mpc) galaxies with resolved (5″–18″; 90 pc–1 kpc) imaging polarimetric observations using SOFIA/HAWC+ from 53 to 214 μm. We compute the magnetic pitch-angle (Ψ_B) profiles as a function of the galactocentric radius. We introduce a new magnetic alignment parameter (ζ) to estimate the disordered-to-ordered ratio of spiral B-fields. We find FIR and radio wavelengths to not generally trace the same B-field morphology in galaxies. The Ψ_B profiles tend to be more ordered across all galactocentric radii in radio ($\zeta_{6cm} = 0.93 \pm 0.03$) than in FIR ($\zeta_{154\mu m} = 0.84 \pm 0.14$). For spiral galaxies, FIR B-fields are 2%–75% more turbulent than the radio B-fields. For starburst galaxies, we find that FIR polarization is a better tracer of the B-fields along the galactic outflows than radio polarization. Our results suggest that the B-fields associated with dense, dusty, turbulent star-forming regions (those traced at FIR) are less ordered than warmer, less dense regions (those traced at radio) of the interstellar medium. The FIR B-fields seem to be more sensitive to the activity of the star-forming regions and molecular clouds within a vertical height of a few hundred parsecs in the disk of spiral galaxies than the radio B-fields.

Unified Astronomy Thesaurus concepts: Astrophysical magnetism (102); Extragalactic magnetic fields (507); Polarimetry (1278); Dust continuum emission (412); Radio continuum emission (1340); Galaxy evolution (594); Spiral galaxies (1560); Disk galaxies (391)

1. Introduction

Polarimetric observations allow the tracing of magnetic fields (B-field) in galaxies (e.g., Beck & Wielebinski 2013). Synchrotron emission is expected to emerge largely from the warm and diffuse interstellar medium (ISM), due to a combination of a large volume fraction for the ubiquitous cosmic-ray electron population and thermal gas emission. While this emission is considerably sensitive to Faraday rotation, it should be relatively less affected by depolarization from disordered B-field structures owing to larger coherence scales for the field and a prevalence of the mean magnetic field (Evirgen et al. 2017). The far-infrared (FIR) polarization arises from thermal emission of magnetically aligned dust grains tracing a weighted density medium along the line of sight (LOS). Based on the 2.7 m Stratospheric Observatory For Infrared Astronomy (SOFIA)/ HAWC+ observations of extragalactic objects, we estimate that this polarized FIR emission is associated with a relatively dense ($\log_{10}(N_{\mathrm{HI+H_2}}\,[\mathrm{cm}^{-2}]) = [20, 23]$) and cold ($T_d = [20, 50]$ K) component of the ISM (Lopez-Rodriguez et al. 2022b; SALSA IV). The addition of FIR polarimetric observations by the Survey of extragALactic magnetiSm with SOFIA (SALSA; PI: E. Lopez-Rodriguez & S. A. Mao) Legacy Program (Lopez-Rodriguez et al. 2022b, SALSA IV) enables us for the first time to explore the differences with radio polarimetric observations, allowing us to investigate extragalactic B-fields in different ISM phases (Figure 1).
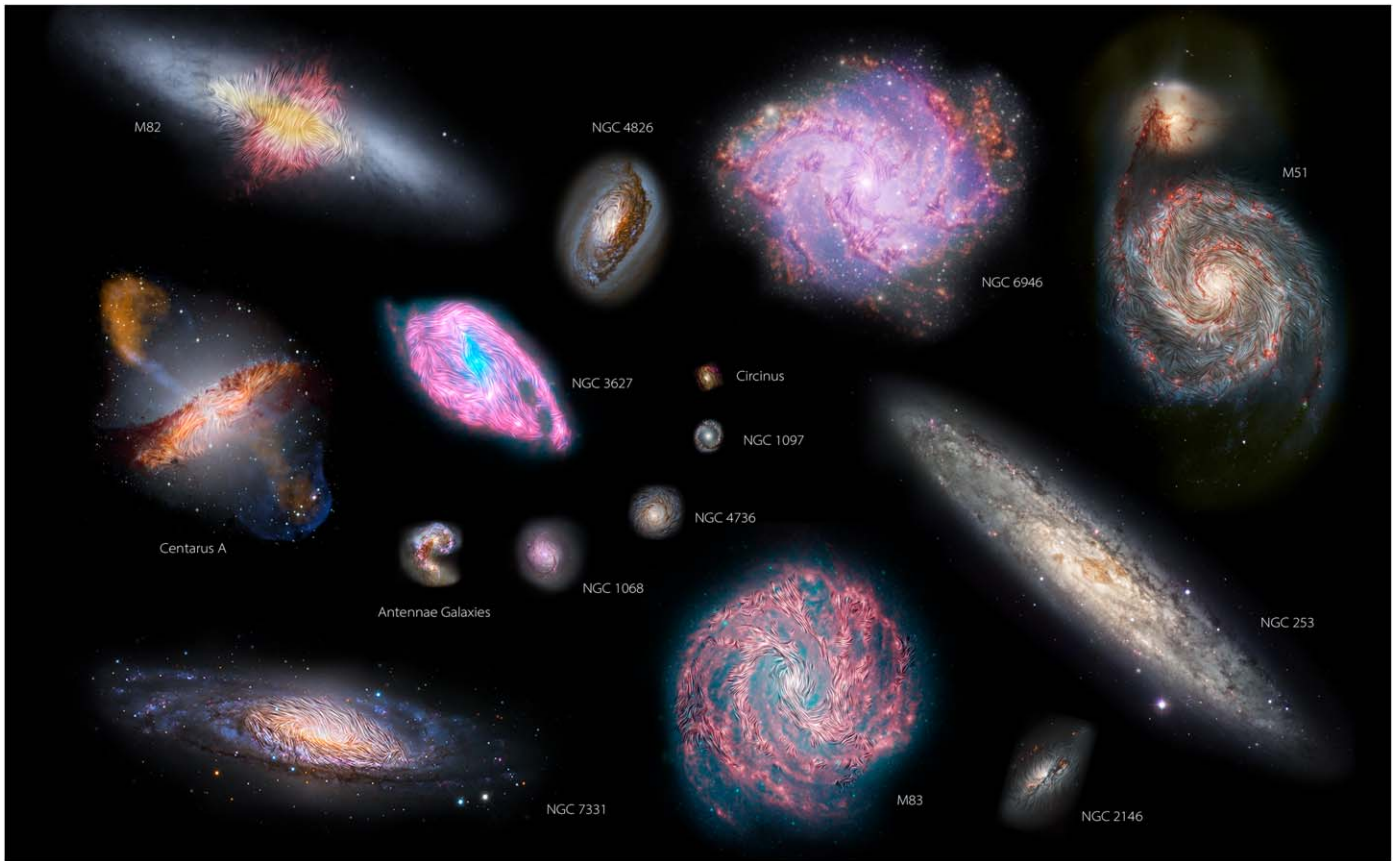
Figure 1. FIR magnetic field orientations in the plane of the sky represented over the galaxies in the SALSA sample (including the Antennae galaxies from Lopez-Rodriguez et al. 2023; SALSA VI) using the Line Integral Convolution (LIC; Cabral & Leedom 1993) technique over archival background observations. References to the specific RGB background image of each object are detailed in Appendix C. Objects are shown in relative angular sizes based on SOFIA/HAWC+ limit detection radius. Note that this figure is only for illustrative purposes, and no analysis was derived from it.

In fact, while the large-scale ordered structures of the B-field[18] measured in radio and FIR are compatible in the less dense interarm regions, significant divergence has been found in the spiral arms of M51 (SALSA I; Borlaff et al. 2021; Surgent et al. 2023). This result may be due to the different thermodynamical properties between the warm diffuse ISM and the cold dust filaments associated with star-forming regions and molecular clouds. In the closest merger of two spiral galaxies (the Antennae galaxies), the FIR B-field closely follows the relic spiral arm, while the radio B-field is mostly radial (Lopez-Rodriguez et al. 2023; SALSA VI). This result suggests that the FIR B-field may be cospatial with the molecular gas in the midplane of the relic spiral arm, while the radio B-field seems to be more aligned with the dynamics of the H I gas on an extraplanar layer above the disk affected by the merger activity. In addition, the 1 kpc scale starburst ring of NGC 1097 has a compressed and constant FIR B-field at the intersection with the galactic bar, while the radio B-field has a spiral morphology tightly cospatial with the diffuse neutral gas (Lopez-Rodriguez et al. 2021a; SALSA II). To observe the B-field within the cold and dense ISM affected by the star formation activity and molecular clouds, FIR polarimetric observations are necessary.

In this paper, we explore the structure of the B-field in a quantitative approach probed by the FIR and radio for a sample of 14 galaxies with diverse morphologies (grand-design spirals, post-merger, starbursts). In addition, we will compare the results with the B-field structure measured using radio polarimetric observations for cases in which ancillary data are available (see Section 2.2). Section 3 is dedicated to the analysis of the B-field orientation maps. In Section 4 we quantitatively analyze the structure of the B-field pitch angle for spiral galaxies in the sample. Finally, Section 5 introduces the structural parameter, ζ, dedicated to quantifying the ordering ratio of the spiral B-field. The discussion and conclusions are presented in Sections 6 and 7, respectively.

2. Data

2.1. Far-infrared Polarimetric Observations

We analyze the B-field orientations of the galaxies using the same FIR polarimetric observations as presented in SALSA III and IV (Lopez-Rodriguez et al. 2022a, 2022b). The associated FIR polarimetry data are from the SALSA Legacy Program obtained with the High-Angular Wideband Camera Plus (HAWC+; Vaillancourt et al. 2007; Dowell et al. 2010; Harper et al. 2018) on board SOFIA. SOFIA/HAWC+ has an optimal combination of spatial resolution, field of view (FOV), and sensitivity for observational tests of the theoretical connections

---

[18] *Ordered fields* are defined to be what polarized FIR emission or synchrotron emission at short radio wavelengths (where Faraday depolarization is small) measures within the telescope beam, projected to the plane perpendicular to the LOS. Contributions for ordered fields come from *anisotropic random fields*, whose average over the beam vanishes, and *regular fields*, whose average over the beam is finite. To distinguish between these contributions, additional Faraday rotation data in the radio range are needed (Beck & Wielebinski 2013).

Table 1
HAWC+ Configuration

Band (1)	λ_c (μm) (2)	$\Delta\lambda$ (μm) (3)	Pixel Scale (arcsec) (4)	Beam Size (arcsec) (5)	Polarimetry FOV (arcmin) (6)
A	53	8.7	2.55	4.85	1.4 × 1.7
C	89	17	4.02	7.8	2.1 × 2.7
D	154	34	6.90	13.6	3.7 × 4.6
E	214	44	9.37	18.2	4.2 × 6.2

Note. Column (1): band name. Column (2): central wavelength of the band in μm. Column (3): FWHM bandwidth in μm. Column (4): pixel scale of the band in arcsec. Column (5): FWHM in arcsec. Column (6): FOV for polarimetric observations in arcmin.

between B-field, turbulence, and star formation. FIR polarimetric observations—practically impossible using ground-based observatories owing to atmospheric absorption—allow us to efficiently detect the thermal polarized emission of magnetically aligned dust grains.

In summary, the FIR polarimetric observations were performed using four bands, 53, 89, 154, and 214 μm, with SOFIA/HAWC+. Table 1 shows the HAWC+ configuration for every band. The observations were performed using the on-the-fly-mapping (OTFMAP) polarimetric mode described in SALSA III (Lopez-Rodriguez et al. 2022a). The exception is M51: this galaxy was observed using the chopping and nodding technique and reduced as described by Borlaff et al. (2021). Table 2 shows the galaxy sample and the associated bands. The pixel scale of the final data product is equal to the detector pixel scale (i.e., Nyquist sampling) in any given band (Table 1). For a detailed description of the analysis of the polarization fraction see SALSA IV (Lopez-Rodriguez et al. 2022b). Table 3 shows the properties of the galaxy sample.

2.2. Radio Polarimetric Observations

Ancillary radio polarimetric observations at 3 and 6 cm are used for the analysis. Table 2 shows the radio polarimetric data that were publicly available and kindly shared by the authors of the associated manuscripts. These data sets were obtained using observations of the Effelsberg 100 m single-dish radio-telescope, in combination with data sets from the Karl G. Jansky Very Large Array (VLA) when available. The beam sizes for the radio polarization vary from target to target between $6''$ and $15''$. The physical beam sizes (in pc) of the original available data sets are described in Table 2. We refer to the original manuscripts shown in Table 2 for a complete description of the observations and analysis of the data sets used in our work. Longer-wavelength (18 and 20 cm) observations can be strongly affected by Faraday rotation (Beck et al. 2019) and are thus not considered in this work.

For each galaxy and radio wavelength, the Stokes IQU were convolved with a Gaussian kernel to match the beam size (FWHM) of HAWC+ at the bands shown in Table 2. Then, we reprojected each data set to the largest beam size per galaxy and per band, matching the same pixel scale and FOV. Finally, the fractional degree (P), angle of polarization (PA), and polarized flux (PI) were computed, accounting for the level of polarization bias. To avoid biased results due to the number of measurements across the galaxy, we only use radio polarization measurements that are spatially coincident with the HAWC+ observations. The radio polarization maps are

used to spatially correlate the polarization arising from synchrotron emission with that arising from thermal emission by means of magnetically aligned dust grains observed with HAWC+. Throughout this manuscript, the results at 3 and 6 cm are very similar, within their uncertainties.

3. Magnetic Field Orientation Maps

3.1. Methodology

Figures 2–7 show the B-field orientation maps of the galaxies associated with the first data release of SALSA (SALSA IV; Lopez-Rodriguez et al. 2022b) at FIR wavelengths and radio wavelengths (when available; see Table 2). The FIR polarization measurements with at least $PI/\sigma_{PI} \geqslant 2.0$ and $P \leqslant 20\%$ were selected for all galaxies, with customized I/σ_I to avoid contamination from the background, as shown in Appendix A (Table 5), where σ_{PI} and σ_I are the uncertainties per pixel of the polarized flux density and Stokes I, respectively. The polarization fraction limit of $P = 20\%$ is given by the maximum polarization fraction (p_{max}=19.8%) of interstellar dust measured by Planck observations (Planck Collaboration et al. 2015). Note that more stringent quality cuts were applied to some specific galaxies, to avoid systematic effects. We refer to Lopez-Rodriguez et al. (2021b) for specific information about the quality cuts chosen for each galaxy and its relation to the SOFIA/HAWC+ OTFMAP polarimetric observation mode. We have rotated the measured polarization angles by 90° to show the inferred B-field orientations in the plane of the sky. For radio polarization measurements, all pixels with $PI/\sigma_{PI} \leqslant 2.0$ and $I/\sigma_I \leqslant 2$ were excluded, as well as those pixels that contain no significant FIR polarization emission. For visualization purposes, all figures in this manuscript have a constant polarization length to show the B-field orientation.

Measuring the average B-field orientation allows us to quantify the effects of the different spatial resolutions in the observations. We provide two different estimations of the average B-field position angle: $\langle PA_B^{hist}\rangle$ and $\langle PA_B^{int}\rangle$. $\langle PA_B^{hist}\rangle$ is defined as the average of the B-field position angles of the individual polarization measurements after quality cuts. $\langle PA_B^{hist}\rangle$ is estimated using the circular mean as

$$\langle PA_B^{hist}\rangle = \frac{1}{2}\mathrm{atan2}\left(\sum_{i=1}^{N}\sin(2PA_{B,i}), \sum_{i=1}^{N}\cos(2PA_{B,i})\right), \quad (1)$$

where $PA_{B,i}$ is the B-field orientation of N individual polarization measurements.

$\langle PA_B^{int}\rangle$ is the integrated B-field orientation of the galaxy disk, estimated as

$$\langle PA_B^{int}\rangle = \frac{1}{2}\arctan\left(\frac{\langle U\rangle}{\langle Q\rangle}\right) + \frac{\pi}{2}, \quad (2)$$

where $\langle U\rangle$ and $\langle Q\rangle$ are the average of the Stokes QU for pixels with $I/\sigma_I \geqslant 20$ in the FIR observations.

The difference between $\langle PA_B^{hist}\rangle$ and $\langle PA_B^{int}\rangle$ is that the latter is the average orientation of the B-field in the case of unresolved observations (assigning higher weights to pixels with larger PI). The uncertainty is a measurement of the accuracy of the polarization angle of an unresolved galaxy. In contrast, $\langle PA_B^{hist}\rangle$ is an estimation of the circular mean B-field orientation on all the analyzed independent beams across the galaxy disk, not weighted by PI, allowing us to contrast with $\langle PA_B^{int}\rangle$ how the

Table 2
FIR and Radio Polarimetric Data

Galaxy	FIR (μm)	$\theta_{\mathrm{FIR,beam,pc}}$ (pc)	Radio (cm)	$\theta_{\mathrm{radio,beam,pc}}$ (pc)	References
(1)	(2)	(3)	(4)	(5)	(6)
Centaurus A	89	128	...	...	...
Circinus	53, 89, 214	98, 157, 367	...	...	...
M51	154	566	3, 6	333	Fletcher et al. (2011)
M82	53, 89, 154, 214	91, 146, 254, 340	3 + 6	112	Adebahr et al. (2013, 2017)
M83	154	307	6	226	Frick et al. (2016)
NGC 253	89, 154	132, 231	3, 6	119	Heesen et al. (2011)
NGC 1068	53, 89	335, 539	...	...	...
NGC 1097	89, 154	722, 1259	3, 6	556	Beck et al. (2005)
NGC 2146	53, 89, 154, 214	400, 644, 1123, 1504	...	...	...
NGC 3627	154	587	3, 6	561	Soida et al. (2001)
NGC 4736	154	349	3, 6	206, 385	Chyży & Buta (2008)
NGC 4826	89	210	...	...	...
NGC 6946	154	448	6	495	Beck (1991, 2007)
NGC 7331	154	1025	...	...	...

Note. Column (1): galaxy name. Column (2): central wavelength of the HAWC+ bands. Column (3): physical scale of the beam at each HAWC+ band. Column (4): central wavelength of the band at radio wavelengths. Column (5): physical scale of the beam at each radio band. Column (6): references of the radio polarimetric observations.

average position angle of the polarization maps is modified with sufficient spatial resolution. The uncertainty is a measurement of the angular dispersion of the distribution of B-field orientations within the galaxy disk. The uncertainties of $\langle \mathrm{PA}_B^{\mathrm{int}} \rangle$ and $\langle \mathrm{PA}_B^{\mathrm{hist}} \rangle$ are measured using the definition of circular standard deviation from Mardia (1972), implemented in `SciPy`.[19]

Figure 8 shows the histograms of the B-field orientations in bins of 10° for all the individual polarization measurements per galaxy and per band at FIR (filled histograms) and 6 cm (black solid lines) wavelengths. We show the estimations of $\langle \mathrm{PA}_B^{\mathrm{hist}} \rangle$ per galaxy and per band. The 1σ uncertainty is estimated as the standard deviation of the histogram. As mentioned in Section 2.2, we only use radio polarization measurements that are spatially coincident with the HAWC+ observations. The comparison between $\langle \mathrm{PA}_B^{\mathrm{hist}} \rangle$ and $\langle \mathrm{PA}_B^{\mathrm{int}} \rangle$ for the FIR and radio observations is shown in Figure 9. The tabulated data can be found in Appendix A (Table 5).

3.2. Results

We present the results from the analysis of the morphology of the B-field estimated using FIR and radio observations. We divide our sample (Table 3) into starburst and/or high-inclination galaxies (✴; without a clear spiral pattern, Section 3.2.1) and low-inclination spiral galaxies (◎; with a spiral B-field pattern, Section 3.2.2). In general, some spiral galaxies with lower inclination tend to present well-defined spiral magnetic arms. We use these to measure their magnetic pitch angles. Starburst and edge-on galaxies show multiple B-field components associated with the galactic outflows, if present, and the B-fields parallel to the disk. We note that this classification addresses strictly the projected B-field structure of the objects, which can be different from their respective morphological classification.

---

[19] scipy.stats.circstd: https://docs.scipy.org/doc/scipy/reference/generated/scipy.stats.circstd.html

3.2.1. Starbursts and/or High-inclination Galaxies

Centaurus A (Figure 2) shows a B-field orientation tightly following the 3 kpc warped molecular disk as previously reported by Lopez-Rodriguez (2021). The $\langle \mathrm{PA}_B^{\mathrm{hist}} \rangle$ and $\langle \mathrm{PA}_B^{\mathrm{int}} \rangle$ are measured to be 124° ± 28° and 126° ± 9°, respectively. The large angular dispersion of ±28° is attributed to turbulence at spatial scales smaller than the beam of the observations driven by the merger activity and star-forming regions across the warped molecular disk.

We measure an almost constant B-field orientation within the central 1 kpc of the Circinus galaxy (Figure 3). Note that the B-field orientation bends around the core at all wavelengths, which may indicate that the measured B-field is arising from the central starburst ring (Elmouttie et al. 1998b; Zschaechner et al. 2016). The $\langle \mathrm{PA}_B^{\mathrm{hist}} \rangle$ changes from 52° ± 23° at 53 μm to 28° ± 37° at 89 μm, with a similar (within the uncertainties) $\langle \mathrm{PA}_B^{\mathrm{int}} \rangle$. At 214 μm, the $\langle \mathrm{PA}_B^{\mathrm{int}} \rangle$ is dominated by the highly polarized regions in the bar of the galaxy with a large-scale B-field at 179° ± 2°. The B-field orientation in the central 1 kpc at 214 μm is consistent with the B-field at 53 and 89 μm. Radio polarimetric observations at 6 cm with a beam size of 9″ show two radio lobes cospatial with the ionization cones and a spiral B-field at scales of 1′ north and south of the unpolarized core (Elmouttie et al. 1998a).

We present a new analysis of the 154 μm B-field orientation measurements of NGC 1097. The galaxy shows a constant FIR B-field orientation at 154 μm within the central 1 kpc starburst ring in agreement with the previous B-field orientations reported at 89 μm by Lopez-Rodriguez et al. (2021a; SALSA II). The $\langle \mathrm{PA}_B^{\mathrm{hist}} \rangle$ and $\langle \mathrm{PA}_B^{\mathrm{int}} \rangle$ are measured to be 126° ± 35° and 134° ± 16°, respectively (Table 5). The 154 μm B-field is parallel to the galaxy's bar (which goes from southeast to northwest in the image). The radio polarimetric observations show a spiral B-field pattern within the central 1 kpc of the starburst ring of NGC 1097 (Beck et al. 2005). The differences in the FIR and radio B-fields were suggested to arise from (a) the diffuse gas dragging matter toward the core at radio and (b) the dense gas located in the galactic shocks at the intersections of the bar and starburst ring (Lopez-Rodriguez et al. 2021a).

Table 3
Galaxy Sample

Galaxy	Distance[1] (Mpc)	Scale (pc arcsec^{-1})	Type[a] (deg)	Inclination (i)[2] (deg)	Tilt (θ)[2] (deg)	References
(1)	(2)	(3)	(4)	(5)	(6)	(7)
✳Centaurus A	3.42	16.42	S0pec/Sy2/RG	83 ± 6	114 ± 4	(1) Ferrarese et al. (2007); (2) Quillen et al. (2010)
✳Circinus	4.20	20.17	SA(s)b/Sy2	40 ± 10	205 ± 10	(1) Tully et al. (2009); (2) Jones et al. (1999)
◎M51	8.58	41.21	Sa	22.5 ± 5	−7 ± 3	(1) McQuinn et al. (2017); (2) Colombo et al. (2014)
✳M82	3.85	18.49	I0/Sbrst	76 ± 1	64 ± 1	(1) Vacca et al. (2015); (2) Mayya et al. (2005)
◎M83	4.66	22.38	SAB(s)c	25 ± 5	226 ± 5	(1) Tully et al. (2013); (2) Crosthwaite et al. (2002)
✳NGC 253	3.50	16.81	SAB(s)c/Sbrst	78.3 ± 1.0	52 ± 1	(1) Radburn-Smith et al. (2011); (2) Lucero et al. (2015)
◎NGC 1068	14.40	69.16	(R)SA(rs)b/Sy2	40 ± 3	286 ± 5	(1) Bland-Hawthorn et al. (1997); (2) Brinks et al. (1997)
◎NGC 1097	19.10	92.21	SB(s)b/Sy1	41.7 ± 0.6	133.0 ± 0.1	(1) Willick et al. (1997); (2) Hsieh et al. (2011)
✳NGC 2146	17.20	82.61	SB(s)ab/Sbrst	63 ± 2	140 ± 2	(1) Tully (1988); (2) Tarchi et al. (2004)
◎NGC 3627	8.90	42.75	SAB(s)b	52 ± 1	176 ± 1	(1) Kennicutt et al. (2003); (2) Kuno et al. (2007)
◎NGC 4736	5.3	25.46	SA(r)ab	36 ± 7	292 ± 2	(1) Kennicutt et al. (2003); (2) Dicaire et al. (2008)
◎NGC 4826	5.60	26.89	(R)SA(rs)ab	65 ± 5	125 ± 5	(1) Kennicutt et al. (2003); (2) Braun et al. (1994)
◎NGC 6946	6.80	32.66	Sc	38.4 ± 3.0	239 ± 1	(1) Karachentsev et al. (2000); (2) Daigle et al. (2006)
◎NGC 7331	15.7	75.40	SA(s)b	78.1 ± 2.7	165 ± 1.2	(1) Kennicutt et al. (2003); (2) Daigle et al. (2006)

Note. Column (1): galaxy classification and name. ◎: face-on spiral galaxies with a spiral B-field pattern; ✳: starburst and/or edge-on galaxies without a clear spiral pattern. Column (2): galaxy distance in Mpc. Column (3): physical scale in pc arcsec^{-1}. Column (4): galaxy type. Column (5): inclination of the galaxy in degrees (face-on $i = 0°$, edge-on $i = 90°$). Column (6): position angle of the large axis of the galaxy in the plane of the sky. Column (7): references associated with the distance, inclination, and tilt angles.
[a] Galaxy type from NASA/IPAC Extragalactic Database (NED; https://ned.ipac.caltech.edu/).
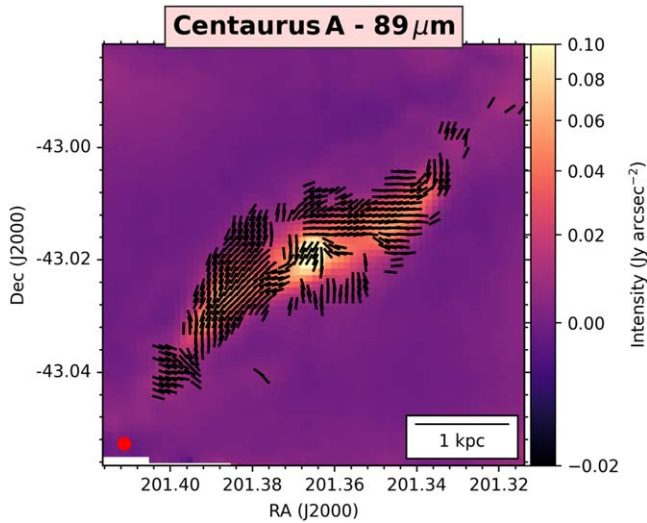
Figure 2. FIR B-field orientation maps of Centaurus A. The color scale shows the surface brightness in FIR (89 μm). Polarization measurements have been set to have a constant length to show the inferred B-field orientation (black dashes). Polarization measurements with $\mathrm{PI}/\sigma_{\mathrm{PI}} \geqslant 2.5$, $P \leqslant 20\%$, and $I/\sigma_I \geqslant 10$ were selected.

The former generates a spiral B-field, and the latter generates a constant B-field in the shocks.

M82's B-field orientation at FIR and radio polarization maps show large morphological differences (Figure 4). The 53–214 μm show a B-field orientation perpendicular to the galaxy's disk indicating the presence of a galactic outflow with a diameter of 1 kpc at the center of the galaxy extending ∼2–3 kpc above and below the galaxy's disk. The B-field orientation is parallel to the disk of the galaxy from a radius of 1–3 kpc. The M82 results are compatible with the previous 53 and 154 μm observations reported by Jones et al. (2019) and Lopez-Rodriguez et al. (2021b). Here we present deeper observations covering a wider wavelength range, i.e., 53–214

μm, and larger extension (>1 kpc). At 3 and 6 cm, the B-field orientation in M82 is mainly parallel to the galactic disk (Adebahr et al. 2017). Depolarization due to Faraday rotation or the lifetime of cosmic-ray electrons along the galactic outflows may cause unpolarized regions (Section 6.3). Interestingly, the radio B-field to the north and south of the galaxy disk is coincident with the B-field orientation at 154 μm (Figure 4).

For NGC 253 (Figure 5), the B-field orientation is predominately parallel to the disk of the galaxy at both 89 and 154 μm. A B-field parallel to the disk of the galaxy at 89 μm was also measured using HAWC+ by Jones et al. (2019). At 89 μm, both $\langle\mathrm{PA}_B^{\mathrm{hist}}\rangle$ and $\langle\mathrm{PA}_B^{\mathrm{int}}\rangle$ are in agreement, within the uncertainties, with a B-field parallel to the disk. However, a change of $\Delta\mathrm{PA}_B = |\langle\mathrm{PA}_B^{\mathrm{int}}\rangle - \langle\mathrm{PA}_B^{\mathrm{hist}}\rangle| = 102° \pm 59°$ is detected at 154 μm. Our hypothesis is that this angular change is mainly due to the highly polarized (∼3%–5%) regions with a B-field twisting within the central 1 kpc of the galaxy with an hourglass shape. This twisted shape may be the signature of the galactic outflow associated with its central starburst having hotter dust temperatures than the dust located in the disk. This B-field structure has also been observed at radio wavelengths (Heesen et al. 2011). Deeper and higher angular resolution observations are required to statistically detect this trend at FIR wavelengths. Note that our released 89 and 154 μm observations only account for 33% and 18% of the total requested time (SALSA III and IV), but these data are deeper and complementary observations to those presented by Jones et al. (2019).

For the starburst galaxy NGC 2146 (Figure 6), the B-field orientation is parallel to the galactic outflow within the 53–154 μm wavelength range. At 53 and 89 μm, the B-field orientation is aligned with the galactic outflow with a diameter of ∼2 kpc at the center of the galaxy. At 214 μm, the B-field orientation is dominated by a component parallel to the disk of the galaxy. The B-field orientation at 154 μm is more complex, showing the transition from a B-field dominated by the galactic outflow
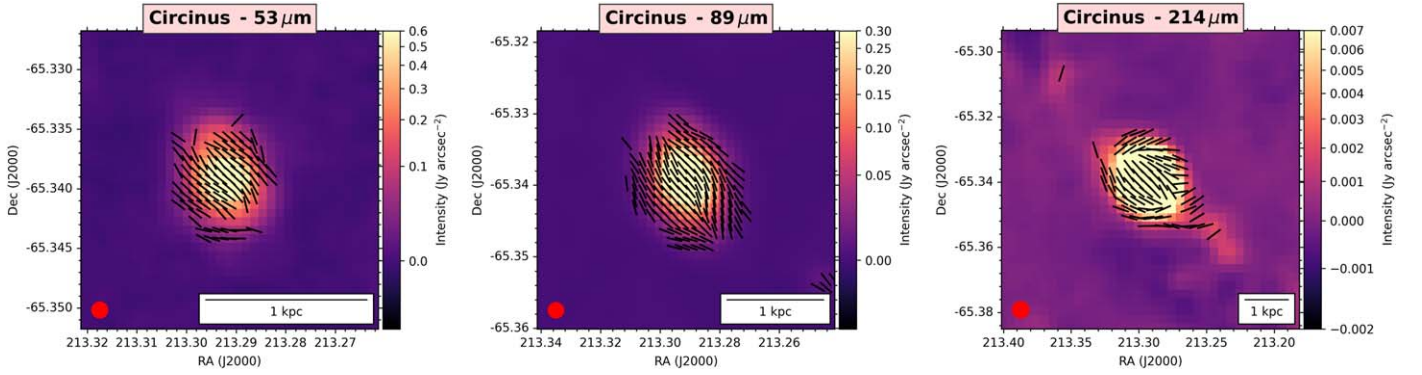
Figure 3. FIR *B*-field orientation maps of Circinus (53, 89, and 214 μm, from left to right). The color scale shows the surface brightness in each band. Polarization measurements have been set to have a constant length to show the inferred *B*-field orientation (black lines). We refer to Table 5 for the quality cuts in PI/σ_{PI}, *P*, and I/σ_I for each band. Note that the FOV is different for each panel, in order to improve the visualization of the individual polarization measurements.

at 53–89 μm to a *B*-field dominated by the galactic disk at 214 μm.

For both M82 and NGC 2146, the histograms show a change in $\langle \mathrm{PA}_B^{hist} \rangle$ and $\langle \mathrm{PA}_B^{int} \rangle$ from 53 to 214 μm (Figure 9 and Table 5). Specifically, $\langle \mathrm{PA}_B^{hist} \rangle$ and $\langle \mathrm{PA}_B^{int} \rangle$ change from $\sim$156° and $\sim$64° (parallel to the outflows) to $\sim$58° and $\sim$120° (parallel to the disk) in M82 and NGC 2146, respectively. These results show that the resolved and unresolved FIR polarimetric observations are sensitive to the *B*-fields in the warm ($\sim$30–50 K at 50–100 μm) dust of galactic outflows and cold ($\sim$10–30 K at 100–220 μm) dust in the galactic disk.

In summary:

1. The edge-on galaxy Centaurus A has a highly inclined *B*-field mostly parallel to the $\sim$3 kpc warped disk of the galaxy. The large-scale *B*-field shows large angular dispersion across the galactic disk driven by the merger and star-forming activity (Lopez-Rodriguez et al. 2021b).
2. The *B*-field orientation in Circinus is mostly constant and parallel to the inner bar and the starburst ring in the central 1 kpc.
3. The starburst galaxies M82, NGC 253, and NGC 2146 show signatures of a *B*-field orientation potentially associated with and parallel to galactic outflows up to $\sim$3 kpc scales above and below the disk. For M82, the *B*-field is parallel to the galactic outflow at all wavelengths (Jones et al. 2019; Lopez-Rodriguez 2021). The median orientation of the FIR *B*-field of NGC 2146 changes with wavelength from parallel (53–89 μm) to perpendicular (154–214 μm) with respect to the galactic outflow driven by the central starburst. For NGC 253, the *B*-field is mostly parallel to the galaxy disk with a signature of an hourglass shape driven by the starburst activity in the central 1 kpc.
4. For M82, the radio *B*-field orientation is parallel to the galaxy disk, although some hint of the galactic outflow is also measured and coincident with the 154 μm *B*-field.

3.2.2. *Spiral Galaxies*

The FIR *B*-field orientation maps of the spiral galaxies are shown in Figure 7 (including NGC 1097). The histograms of *B*-field orientations for the polarization measurements are presented in Figure 8. In general, we find that low-inclination objects (i.e., NGC 1068, NGC 4736, NGC 6946) present relatively flatter PA$_B$ distributions at FIR and radio

wavelengths than galaxies with higher inclinations (i.e., M82, NGC 253, NGC 2146). This result is because the spiral *B*-field is more centrosymmetric at lower inclinations, while the spiral *B*-field is more asymmetric owing to the cancellation of *B*-field along the LOS as inclination increases (see Section 5.3 by Lopez-Rodriguez et al. 2022b).

All galaxies show a large-scale spiral *B*-field, except for NGC 6946, which shows a highly disordered FIR *B*-field spatially located with the star-forming regions in the spiral arms. Figure 7 shows the NGC 6946 *B*-field pattern traced by both FIR and radio polarimetric observations, revealing clear large structural differences. At radio wavelengths, a large-scale well-ordered spiral *B*-field has been measured (Beck 1991, 2007), mostly aligned with the interarm regions ("magnetic arms"), instead of the morphological spiral arms. However, we detect signs of a spiral pattern in radio and FIR also in the morphological spiral arms (see Section 4). At FIR wavelengths, we detect a spiral *B*-field in the central $\sim$3 kpc diameter. At larger galactocentric radius ($R > 3$ kpc), the *B*-field orientation is highly disordered in the spiral arms. The histogram of *B*-field orientations (Figure 8) shows an almost flat distribution with a $\langle \mathrm{PA}_B^{hist,FIR} \rangle = 151° \pm 55°$ at 154 μm and $\langle \mathrm{PA}_B^{hist,Radio} \rangle = 48° \pm 49°$ at 6 cm.

Another remarkable result is the well-ordered $\sim$1 kpc scale spiral *B*-field over the starburst ring of NGC 4736 at both FIR and radio wavelengths (Figure 7). For both tracers, the measured spiral *B*-field seems to be uncorrelated with the underlying morphological structure. We measure a similar $\langle \mathrm{PA}_B^{hist} \rangle$ of $85° \pm 42°$ and $70° \pm 46°$ at 154 μm and 6 cm, respectively. We note that the southern region of the galaxy has slightly different *B*-field orientations at radio and FIR wavelengths, while in the northern region both FIR and radio wavelengths have similar *B*-field orientations. Sections 4 and 5 present a quantification of these differences.

NGC 3627 presents a well-ordered spiral *B*-field that follows the inner morphological spiral pattern at 154 μm, 3 cm, and 6 cm. Interestingly, beyond 90″ from the galactic center, the FIR magnetic orientation deviates from the morphological arms (see northeast region), as opposed to the observed structure in 3 and 6 cm. In Section 4 we will analyze in detail how this change in orientation translates into a break in the magnetic pitch-angle profile very similar to the results obtained in M51 (Borlaff et al. 2021).

We detect a spiral *B*-field morphology in both NGC 4826 and NGC 7331. For each galaxy, the $\langle \mathrm{PA}_B^{hist} \rangle$ and $\langle \mathrm{PA}_B^{int} \rangle$ are in
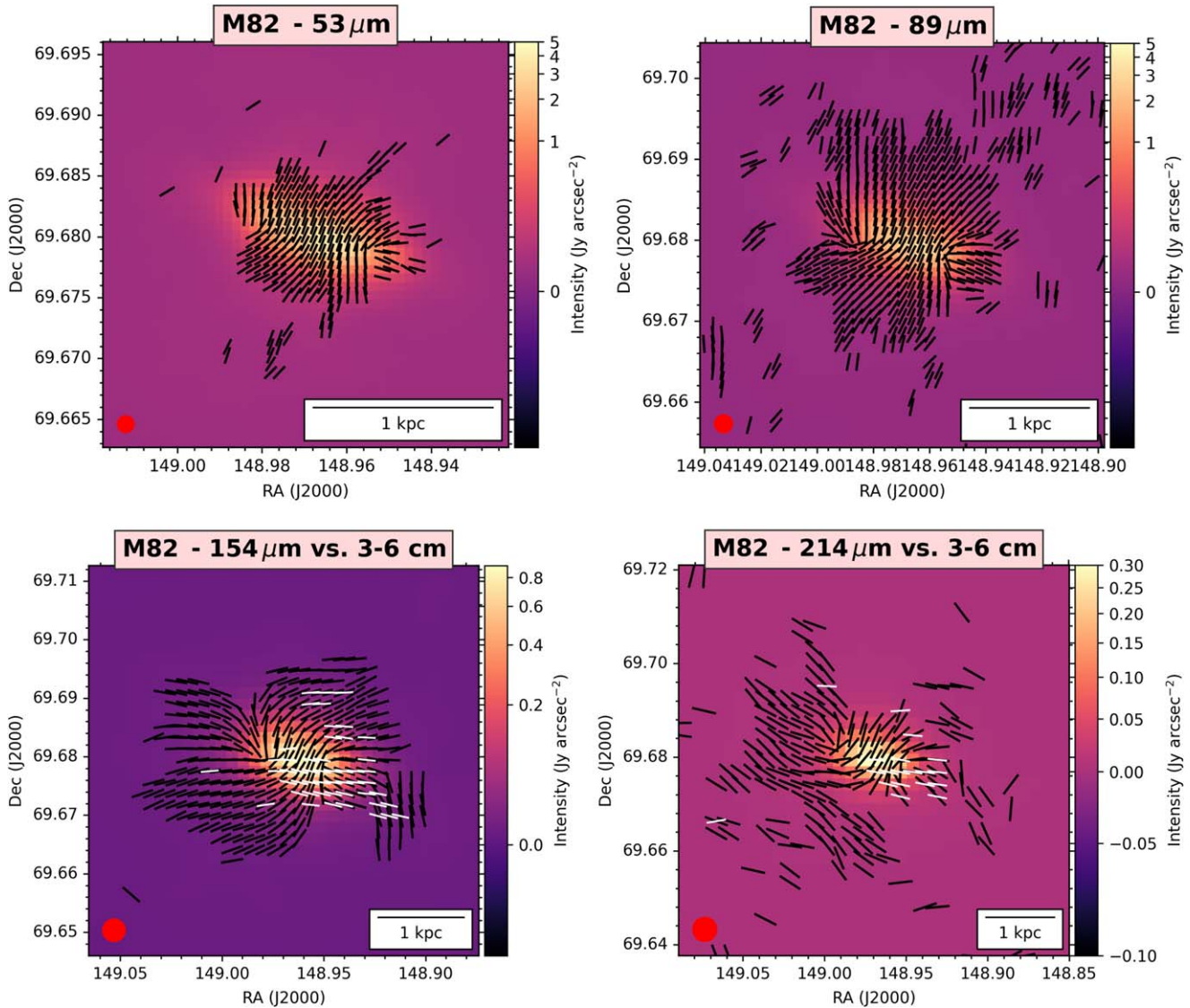
Figure 4. FIR *B*-field orientation maps of M82 (53, 89, 154, and 214 *μ*m, from left to right, top to bottom). The maps in 154 and 214 *μ*m show the radio polarimetric observations from Adebahr et al. (2013, 2017) in 3 and 6 cm (averaged). The color scale shows the surface brightness in each band. Polarization measurements have been set to have a constant length to show the inferred *B*-field orientation (black lines), while the radio polarization observations are represented with white lines. We refer to Table 5 for the quality cuts in PI/σ_{PI}, *P*, and *I*/σ_I for each band. Note that the FOV is different for each panel, in order to improve the visualization of the individual polarization measurements.

agreement, within their uncertainties (Table 5), which indicates that the *B*-field is aligned with the major axis of the galaxy. This result is due to the high inclination (>65°) of these galaxies. NGC 4826 presents a nonregular spiral *B*-field, with the majority of the polarization measurements located in the southern half of the galaxy. Interestingly, only the southern section was found to be polarized also in 18 and 22 cm by Heald et al. (2009), a potential consequence of Faraday depolarization. Section 4 shows the associated radial profiles of the magnetic pitch angles of these galaxies. Radio polarimetric observations covering the several-kiloparsec scale of the host galaxy of NGC 7331 are unavailable.

For M51 and M83, the overall spiral *B*-field morphology is the same in both FIR and radio polarimetric observations, with some significant differences at large radii. The *B*-field orientation map of M51 is the same as presented by Borlaff et al. (2021), where the pitch angles of the spiral arms at the outskirts of M51 are different at FIR and radio

wavelengths. Section 4 shows the associated radial profiles of the magnetic pitch angles of these galaxies. A similar result is observed in the outskirts of M83 when comparing the radio polarization and FIR magnetic pitch-angle profiles (Figure 7).

The *B*-field orientation in NGC 1068 is compatible with the previous 89 *μ*m observations reported by Lopez-Rodriguez et al. (2020). Here we present deeper 89 *μ*m polarimetric observations and new 53 *μ*m polarimetric observations. We detect a 6 kpc scale spiral *B*-field at 89 *μ*m, in comparison with the 3 kpc scale detected by Lopez-Rodriguez et al. (2020). The new 53 *μ*m polarimetric observations show a change of ∼90° at the core of NGC 1068 with respect to the 89 *μ*m. This angular offset may be due to a transition from dichroic absorption to dichroic emission or the fact that the 53 *μ*m is resolving the beginning of the spiral arm within the central 1 kpc.

In summary:
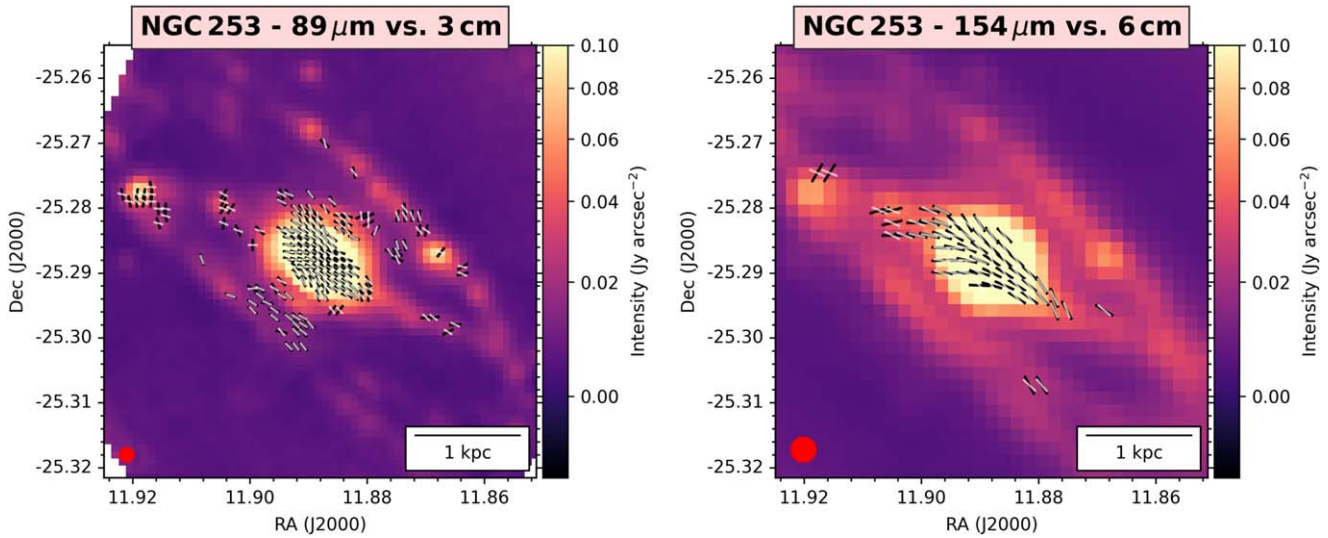
Figure 5. FIR and radio *B*-field orientation maps of NGC 253 (89 μm vs. 3 cm and 154 μm vs. 6 cm, from left to right). The FIR *B*-field is represented with black lines, while the radio polarization observations (Heesen et al. 2011) are represented with white lines. The color scale shows the surface brightness in each band. The polarization vectors have been set to a constant length to show the inferred *B*-field orientation. We refer to Table 5 for the quality cuts in PI/$\sigma_{\rm PI}$, *P*, and *I*/σ_I for each band.
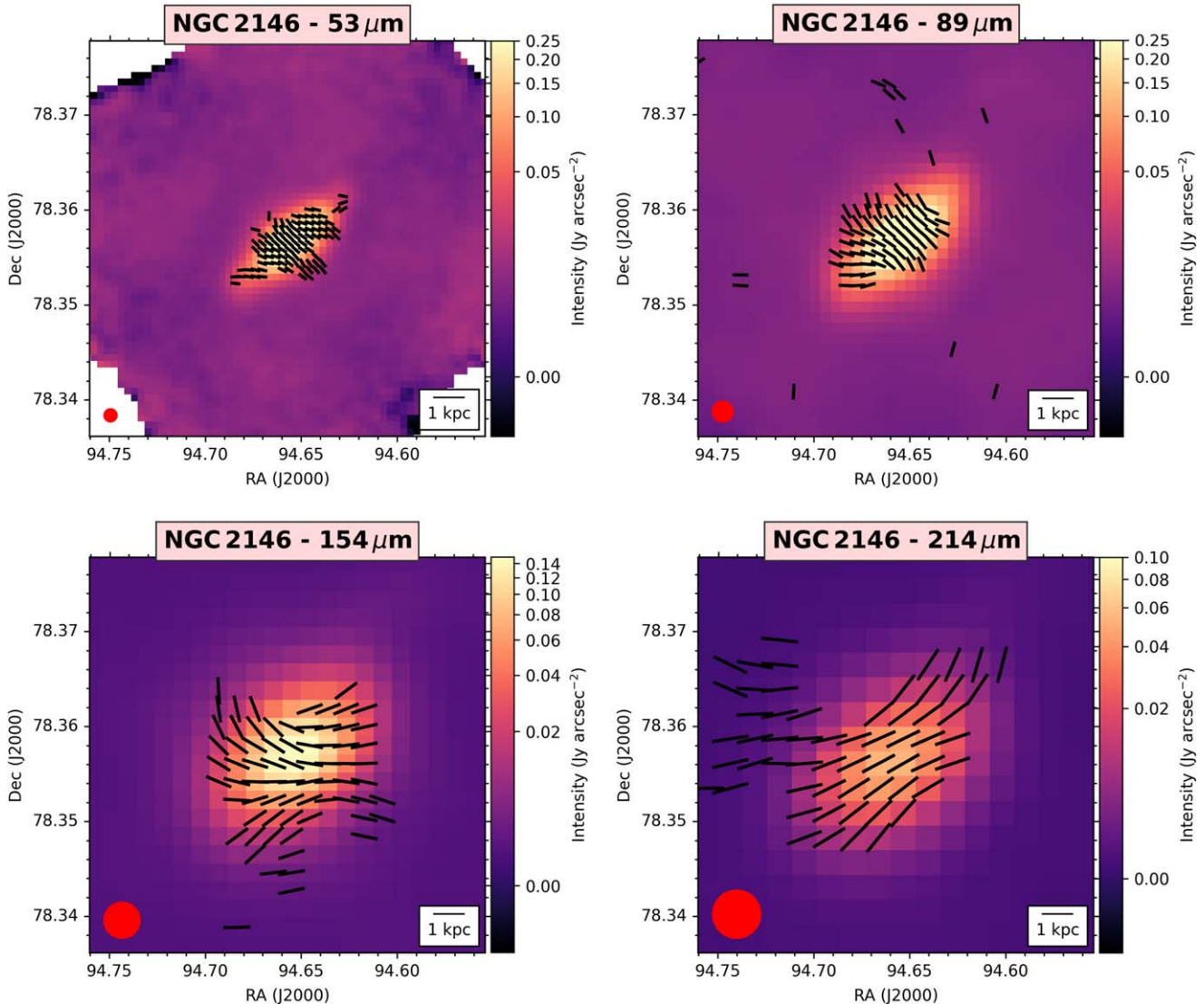
Figure 6. FIR and radio *B*-field orientation maps of NGC 2146 (53, 89, 154, 214 μm, from left to right). FIR *B*-field is represented with black lines. The color scale shows the surface brightness in each band. Polarization measurements have been set to have a constant length to show the inferred *B*-field orientation. Measurements with PI/$\sigma_{\rm PI} \geqslant 3.0$, $P \leqslant 20\%$, and $I/\sigma_I \geqslant 20$ were selected.
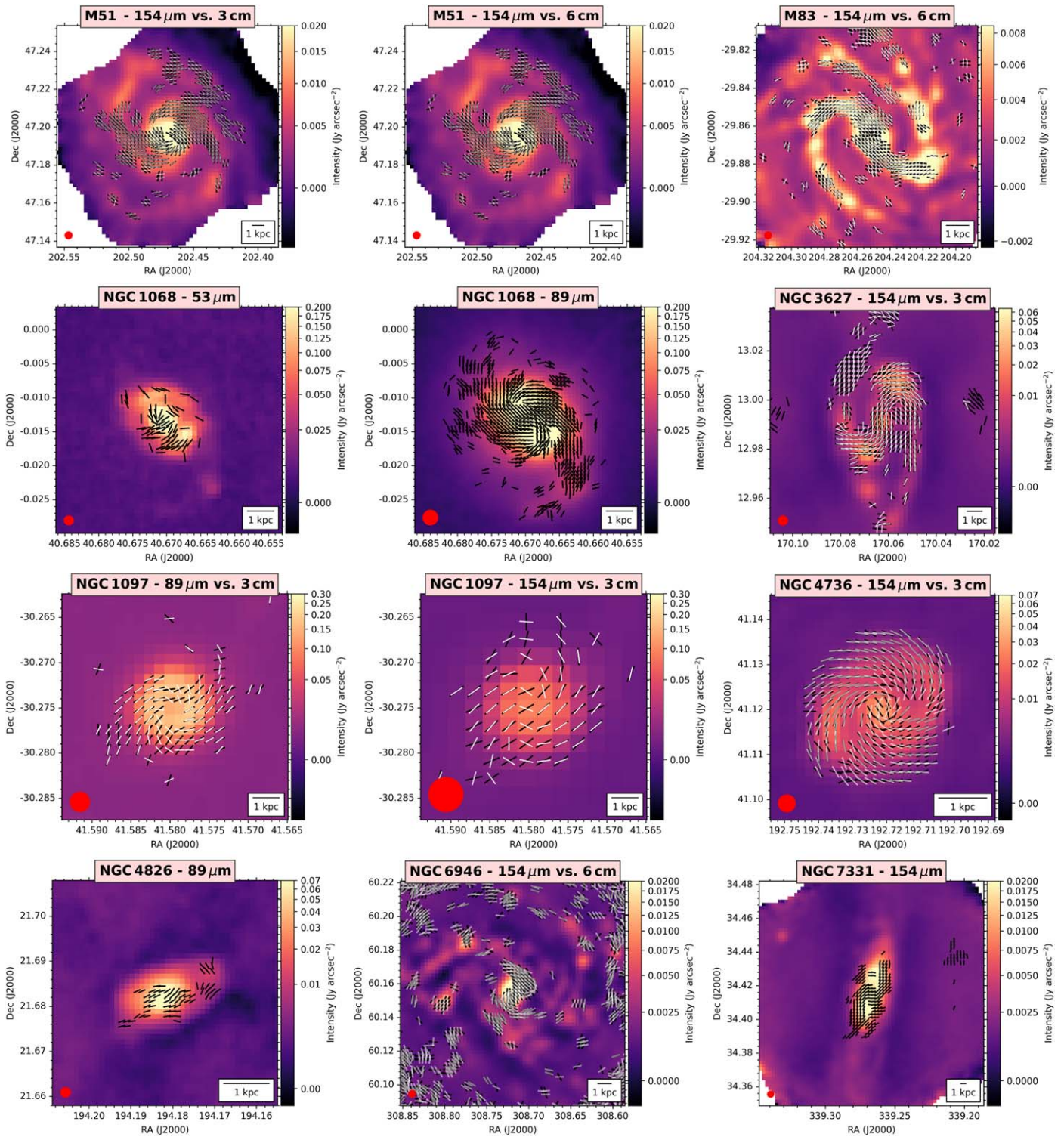
Figure 7. FIR and radio *B*-field orientation maps of the spiral galaxies. From left to right, top to bottom: M51, M83, NGC 1068, NGC 3627, NGC 1097, NGC 4736, NGC 4826, NGC 6946, and NGC 7331 (wavelengths indicated in the titles). FIR *B*-field (53, 89, 154, and 214 μm) is represented with black lines, while radio polarization observations (3, 6 cm) are represented with white lines, if available (see Table 2). The color scale shows the surface brightness in each band. Polarization measurements have been set to have a constant length to show the inferred *B*-field orientation. Measurements with $PI/\sigma_{PI} \geqslant 2.0$, $P \leqslant 20\%$, and $I/\sigma_I \geqslant 20$ were selected.

1. The spiral galaxies M51, M83, NGC 1068, NGC 3627, and NGC 4736 have kiloparsec-scale spiral ordered *B*-fields.

2. NGC 4736 has an FIR and radio spiral *B*-field without clear spatial correspondence with the underlying morphology in total emission. The total emission is cospatial with the starburst ring at ~1 kpc around the core.

3. NGC 6946 has a highly disordered FIR *B*-field, in comparison with the well-ordered large-scale spiral
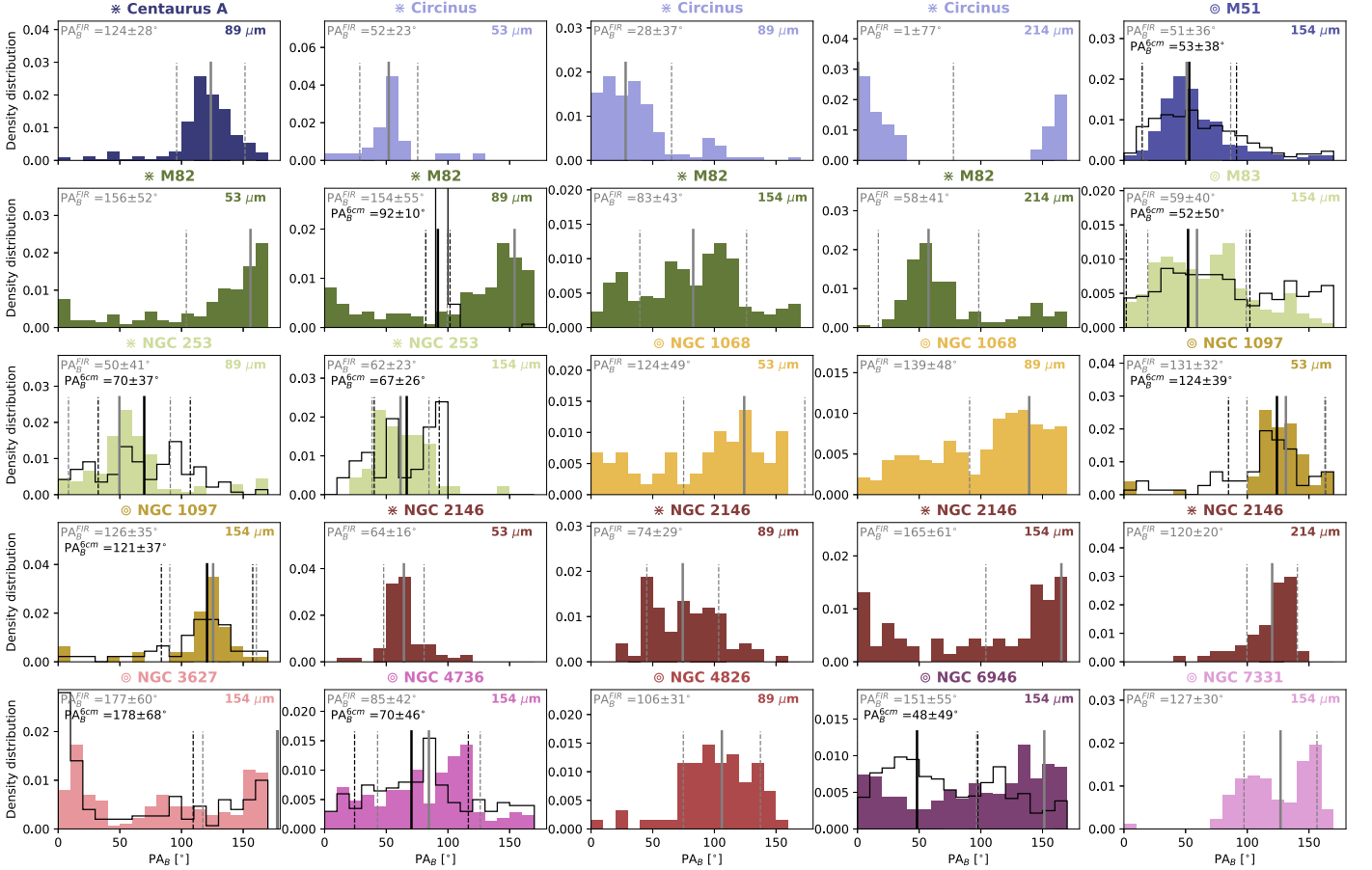
**Figure 8.** Histograms of the *B*-field orientations. The histograms are set to 10° bins, each galaxy is shown in a unique color with the symbols as in Table 3, and the mean (gray solid line, Equation (1)) and 1σ uncertainty (gray dashed line) for the FIR observations are shown. For the galaxies with radio polarimetric observations, the histograms of the *B*-field orientations at 6 cm (black step histogram) with the mean (black solid line, Equation (1)) and 1σ uncertainty (black dashed line) are shown. Note that the radio observations were smoothed to match the HAWC+ observations at each band.

B-field at radio wavelengths. The disordered FIR *B*-field seems to be potentially connected to star formation activity in the spiral arms.

4. Significant large-scale differences between FIR and radio polarization observations are found in several regions of M51, NGC 1097, and NGC 3627.

5. For all these galaxies, deviations from the large-scale spiral *B*-fields are found in star-forming regions and at the edges of the nuclear bar.
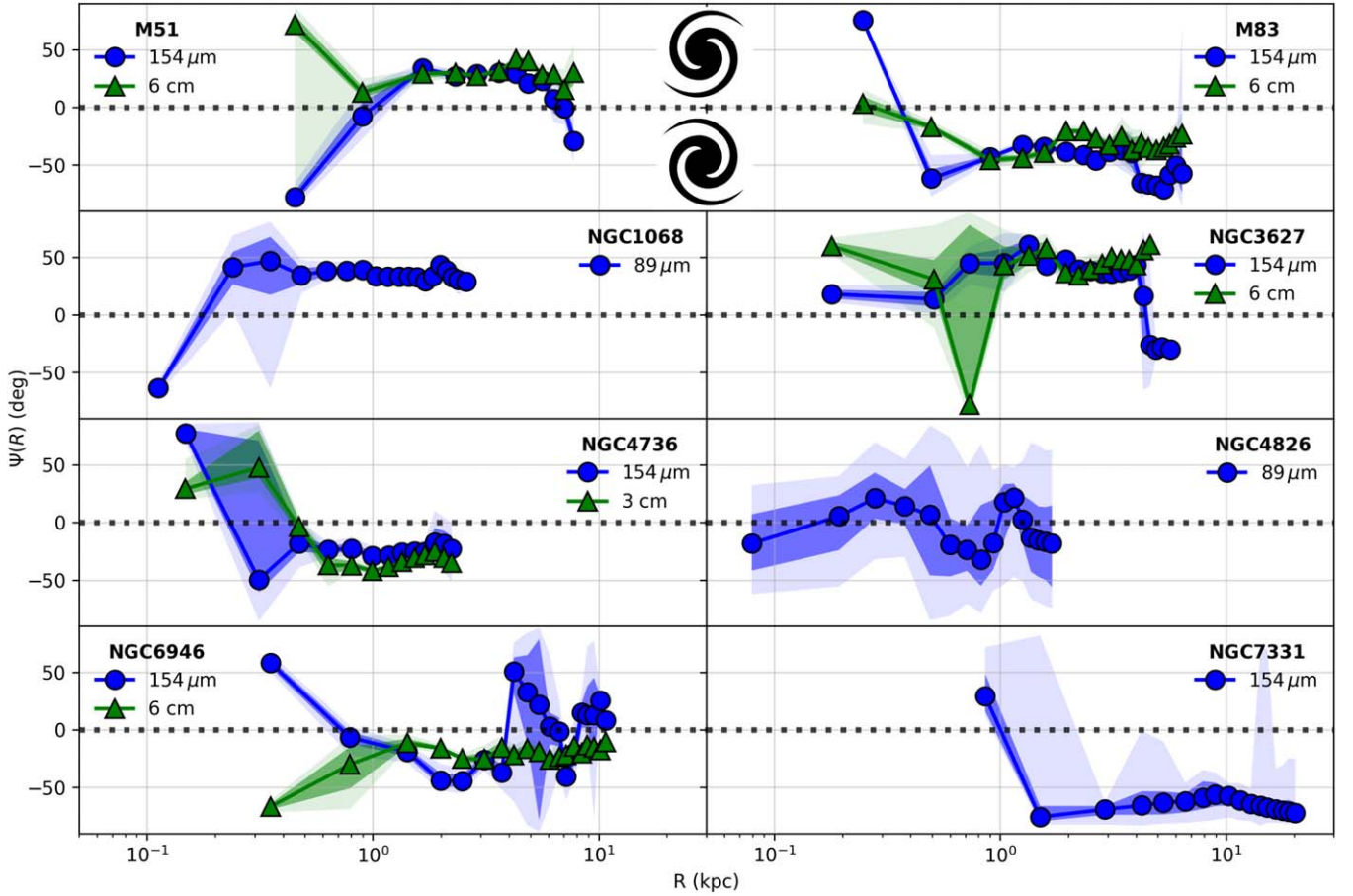
4. Magnetic Pitch Angles

The morphology of the large-scale *B*-field in the disk of spiral galaxies is typically defined using the pitch angle $\Psi_B = \arctan(B_r/B_\phi)$, where B_r is the radial *B*-field component and B_ϕ is the azimuthal *B*-field component (e.g., Krasheninnikova et al. 1989). Note that the *B*-field is three-dimensional, so from an observational point of view these two quantities are the *B*-field components projected on the plane of the sky. Observationally, Ψ_B is defined as the angle between the line tangent to a circle in the galaxy plane and the direction of the *B*-field at a specified radius. Positive values of Ψ_B represent a clockwise sense of the spiral structure, while negative values represent a counterclockwise direction. Values of Ψ_B close to zero represent a circular *B*-field (tightly wound), while higher absolute values of Ψ represent a more open (less wound) spiral
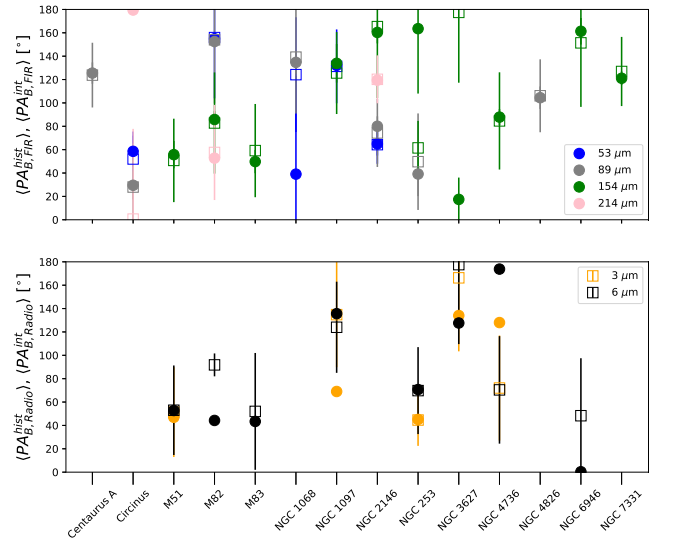
Figure 9. Mean and integrated *B*-field orientation of galaxies. *B*-field orientations at FIR (top) and radio (bottom) from individual measurements, $\langle \mathrm{PA}_B^{hist} \rangle$ (open square, Equation (1)), and from the integrated Stokes QU, $\langle \mathrm{PA}_B^{int} \rangle$ (filled circle, Equation (2)) are shown. Tabulated values are shown in Table 5.

structure. The methodology to estimate the magnetic pitch-angle maps for FIR and radio polarization observations (Mohawc) is described in Appendix B and was previously

Figure 10. Radial profiles of the magnetic pitch angle (Ψ_B) of spiral galaxies at FIR (blue) and radio (green) wavelengths. The 68% (1σ) and 95% (2σ) statistical significance error contours are shown as shaded areas.

presented by Borlaff et al. (2021). This method was implemented in PYTHON and is available on the project website.[20]

We compute the magnetic pitch angles of eight spiral galaxies, M51, M83, NGC 1068, NGC 3627, NGC 4736, NGC 4826, NGC 6946, and NGC 7331. The other galaxies have (a) vertical B-fields along the galactic outflows (i.e., M82, NGC 253, and NGC 2146), (b) parallel B-fields along the galactic disk in edge-on galaxies (i.e., Centaurus A), or (c) constant B-fields in the central 1 kpc (i.e., Circinus, NGC 1097). For these galaxies, we do not perform any analysis based on the magnetic pitch angles with the exception of the global B-field orientation histograms and integrated B-field orientation in the full disk of galaxies as described in Section 3.

Figure 10 shows the magnetic pitch angles as a function of the galactocentric radius at FIR, $\Psi_B^{\rm FIR}$, of the sample of spiral galaxies. Our FIR observations trace the B-fields from 0.1 to 5 kpc in radius for most galaxies and up to 15 kpc in NGC 7331. We also compute the magnetic pitch angles at 3 and 6 cm, $\Psi_B^{\rm Radio}$, whenever available, using the same LOS measurements as those at FIR wavelengths. Table 4 shows the median magnetic pitch angles across the full galaxy disk.

The main result is that FIR and radio wavelengths do not generally trace the same B-field morphology in spiral galaxies. This result has also been recently measured by independent

analyses, using alternative pitch-angle estimation methods (Surgent et al. 2023). As reported in Borlaff et al. (2021), M51's spiral magnetic field presents a similar structure in both radio and FIR within the central 5 kpc, showing a significant difference in the outskirts of the disk. At radii $R > 5$ kpc, a tightening of the FIR spiral magnetic field is observed ($\overline{\Psi_B}$ in FIR changes from approximately $25°$ to $0°$ and negative values). This reduction of the FIR pitch angle is not observed in radio, which displays a pitch angle that opens up with galactocentric radius. Similar discrepancies between FIR and radio B-field structure are observed in the outskirts of M83. M83's FIR polarization structure is more loosely wound than at radio wavelengths (average $\overline{\Psi_B} = -39.9^{+2.2}_{-3.3}°$ at 154 μm and $\overline{\Psi_B} = -29.7^{+3.6}_{-3.9}°$ at 6 cm), and there is a trend toward more negative values in FIR not detected in radio. This behavior is opposite to what is observed in NGC 3627 ($\overline{\Psi_B} = -38.2^{+1.2}_{-1.3}°$ at 154 μm and $\overline{\Psi_B} = -47.71^{+0.13}_{-0.01}°$ at 6 cm) and in the outskirts of M51 ($R > 5$ kpc).

NGC 4736 has a similar spiral B-field orientation in both FIR and radio wavelengths ($\overline{\Psi_B} = -25.33^{+1.51}_{-0.66}°$ at 154 μm and $\overline{\Psi_B} = -35.0^{+4.2}_{-2.3}°$ at 3 cm) within the central 2 kpc. As shown in Figure 7, the northern spiral arm of NGC 4736 has similar pitch angles in both FIR and radio wavelengths. However, the southern arm has a more tightly wound magnetic pitch angle at FIR than at radio wavelengths.

The lack of a well-ordered spiral magnetic structure in NGC 6946 at FIR wavelengths is clear in the magnetic pitch-angle profile. NGC 6946 has a regular B-field at radio

---

[20] Mohawc: https://github.com/Borlaff/MOHAWC

wavelengths ($\Psi^{6\,cm} = -17.6^{+1.7°}_{-4.1}$) and a mostly random one at FIR wavelengths, although signs of a certain spiral structure can be detected with high variability ($\Psi^{FIR} = -6.5^{+5.0°}_{-12.5}$). The B-field morphology at FIR wavelengths is very patchy and mostly coincident with compact regions of high FIR emission, potentially associated with star-forming regions across the disk (SALSA IV; Lopez-Rodriguez et al. 2022b). This result is in contrast to the regular spiral B-field ("magnetic arms") observed at radio wavelengths (Beck 1991, 2007). The difference between the radio polarization pattern and the FIR observations is clearly visible in Figure 7.

For those galaxies without radio polarimetric observations, we found that (a) the highly inclined galaxies NGC 4826 ($\overline{\Psi_B} = -5^{+12°}_{-11}$ at 89 μm) and NGC 7331 ($\overline{\Psi_B} = -66.0^{+1.9°}_{-2.8}$ at 154 μm) have an ordered spiral B-field morphology at FIR wavelengths and (b) the spiral galaxy NGC 1068 ($\overline{\Psi_B} = 33.23^{+0.43°}_{-0.13}$ at 89 μm) has a magnetic pitch angle that is more tightly wound with increasing galactocentric radius ($\rho = -0.618$, $p = 0.006$, Spearman correlation test).

In summary:

1. FIR and radio wavelengths do not generally trace the same B-field morphology in spiral galaxies.
2. Magnetic pitch-angle profiles traced with radio polarization observations present a more constant distribution across the disk than those obtained with FIR (e.g., the outskirts of M51, M83, or the entire disk of NGC 6946).
3. NGC 6946 has a large-scale well-ordered spiral B-field at radio wavelengths, while the B-field is highly disordered at FIR wavelengths. The FIR polarization is mainly cospatial with the star-forming regions, while the radio polarization is cospatial with the morphological interarm regions.

5. Angular Dispersion

5.1. Methodology

Another interesting quantity is the dispersion of the local B-field orientation and the average magnetic pitch angle at each galactocentric radius. In addition to the magnetic pitch angle, Mohawc calculates the residuals between the magnetic pitch-angle model and the measured B-field orientation maps on a pixel-by-pixel basis. These residuals can be used to provide a quantitative measurement of the goodness of fit for the axisymmetric spiral B-field model and, by extension, to compare how "ordered" are the magnetic fields as a function of the tracer. By doing so, we can determine which regions are dominated by large-scale ordered spiral magnetic fields (low residuals) or by "disordered" B-fields (high residuals).[21] We define the magnetic alignment parameter, ζ, as

$$\zeta = \cos(2\delta\theta), \qquad (3)$$

where $\delta\theta$ is defined in Equation (15) from Clark & Hensley (2019) as the angle difference from two angular measurements,

θ₁ and θ₂,

$$\delta\theta = \frac{1}{2}\arctan\left[\frac{\sin(2\theta_1)\cos(2\theta_2) - \cos(2\theta_1)\sin(2\theta_2)}{\cos(2\theta_1)\cos(2\theta_2) + \sin(2\theta_1)\sin(2\theta_2)}\right]. \qquad (4)$$

ζ can range from 1 (perfect alignment) to -1 (perpendicular fields).[22] $\zeta = 1$ thus represents a perfect alignment of the median axisymmetric spiral B-field with the local field (large-scale B-field dominates). A random polarization field (disordered dominated) will yield an average value of $\zeta = 0$. Since the axisymmetric model is measured from the polarization maps, $\zeta = -1$ values are not expected unless extreme small-scale local changes in the B-field direction are present.

The ζ radial profiles can be constructed using the same method as the magnetic pitch-angle profiles (see Appendix B). We use the pitch-angle probability distribution of each pixel to calculate ζ as a function of the galactocentric radius and the associated uncertainties (68%, 95%, equivalent to 1σ, 2σ). For all the analyses, we consider a critical level of at least $p = 0.05$ (95%) to declare statistical significance. This method is implemented in PYTHON and is available on the project website. Most of the large-ζ regions are usually at the cores as expected given the limited statistics within the central two to three beams. Low alignment for the inner beams can be caused by statistical limitations (low number of valid pixels at the core), observational limitations (beam depolarization), and intrinsic physical properties of the core (higher turbulence). Due to this, we remove the central two to three beams for the analysis.

5.2. Results

Figure 11 shows the ζ maps of spiral galaxies on a pixel-by-pixel basis at FIR and radio wavelengths. Figure 12 presents the ζ profiles of magnetic alignment as a function of galactocentric radius for all spiral galaxies in FIR and radio when available. To compare the magnetic alignment profiles as a function of wavelength (Figure 13), we show the histograms of the difference between radio and FIR, calculated as the difference between the ζ maps from Figure 11. The median and 1σ uncertainty of the histogram are shown in each plot and Table 4.

We measure $\zeta > 0.8$ in the majority of the disks of the spiral galaxies of our sample beyond a certain galactocentric radius in both FIR and radio wavelengths (Figure 12), with the exception of NGC 6946 and NGC 3627. This result indicates that a large-scale axisymmetric ordered B-field is the dominant B-field structure in the disk of galaxies at both FIR and radio wavelengths. Note that the individual ζ measurements per LOS at the two wavelength regimes may differ.

The ζ profiles in Figure 12 show that in the analyzed spiral galaxies with radio and FIR data the magnetic alignment at FIR wavelengths tends to be systematically lower than at radio wavelengths at the same radii, with some exceptions in the inner regions of NGC 3627 and NGC 4736. We quantify this result by analyzing the difference between radio and FIR alignment maps ($\Delta\zeta$ is the percent increase of ζ_{FIR} over ζ_{Radio}) in Figure 13. The average values of ζ are always statistically larger in radio polarization observations than FIR when

---

[21] Note that we use the term "disordered" rather than turbulent B-fields because "turbulent" is typically defined as the coherence length of the B-field in the ISM of 50–100 pc (Ruzmaikin et al. 1988; Brandenburg & Subramanian 2005; Haverkorn et al. 2008). These scales are well below the physical resolution, $\theta_{beam,pc} = [210, 1025]$ pc (Table 3), of the FIR and radio observations of spiral galaxies and hence cannot contribute to polarized emission.

[22] Note that this definition is different from the histogram of relative orientations (HRO) used to quantify the relative orientation between the morphological structure of molecular clouds and the B-field orientation (e.g., Planck Collaboration et al. 2016; Jow et al. 2018).

Table 4
Magnetic Pitch Angles of Spiral Galaxies

Galaxy	Band (μm)	$\langle \Psi_B^{FIR} \rangle$ (deg)	ζ^{FIR} (%)	Band (cm)	$\langle \Psi_B^{Radio} \rangle$ (deg)	ζ^{Radio} (%)	$\Delta\zeta^{Radio-FIR}$ (%)
(1)	(2)	(3)	(4)	(5)	(6)	(7)	(8)
M51	154	$28.2^{+1.3}_{-40.5}$	$88.7^{+1.2}_{-1.2}$	3 cm	$29.80^{+10.7}_{-5.6}$	$95.28^{+0.62}_{-0.96}$	$+6.4^{+3.0}_{-2.4}$
				6 cm	$29.8^{+10.7}_{-5.6}$	$94.31^{+0.85}_{-0.45}$	$+7.8^{+2.9}_{-2.5}$
M83	154	$-38.4^{+2.3}_{-27.0}$	$80.71^{+0.69}_{-3.4}$	6 cm	$-31.2^{+10.4}_{-6.7}$	$90.5^{+0.5}_{-2.1}$	$+12.7^{+4.2}_{-3.6}$
NGC 1068	89	$33.1^{+5.8}_{-2.7}$	$86.4^{+5.1}_{-5.2}$	...	...	...	...
NGC 3627	154	$36.6^{+8.9}_{-63.2}$	$80.97^{+0.16}_{-1.57}$	6 cm	$47.8^{+9.2}_{-12.8}$	$91.93^{+1.16}_{-0.28}$	$+11.0^{+4.8}_{-3.8}$
NGC 4736	154	$-24.9^{+6.8}_{-4.0}$	$93.6^{+0.1}_{-4.7}$	3 cm	$-34.0^{+33.4}_{-3.4}$	$95.83^{+0.01}_{-0.35}$	$+1.7^{+1.5}_{-1.0}$
NGC 4826	89	-6^{+22}_{-12}	$57.7^{+4.7}_{-4.2}$	...	...	...	...
NGC 6946	154	-6^{+40}_{-31}	51^{+18}_{-18}	6 cm	$-17.4^{+2.5}_{-7.0}$	$88.0^{+1.8}_{-3.9}$	$+76.0^{+6.2}_{-6.2}$
NGC 7331	154	$-66.2^{+7.7}_{-4.0}$	$86.62^{+0.31}_{-1.53}$	...	...	...	...

Note. Column (1): galaxy name. Column (2): FIR wavelength. Column (3): FIR magnetic pitch angle. The errors represent the standard deviation of the pitch-angle profile, not the uncertainties of the average value. Note: these values are estimated from the pitch-angle profile bins (not pixel to pixel), and their uncertainties are intended to represent its large-scale variability. Column (4): average ζ alignment of the FIR spiral magnetic field. Column (5): radio wavelength. Column (6): radio magnetic pitch angle. Column (7): average ζ alignment of the radio spiral magnetic field. Column (8): difference in ζ alignment between the radio and FIR spiral magnetic field.

compared in the same beams. The histograms show that M51, M83, NGC 3627, NGC 4736, and NGC 6946 have a better alignment with the large-scale ordered B-field in radio than in FIR ($\Delta\zeta = [2 - 75]\%$, radio–FIR). We show the average differences $\Delta\zeta$ for each galaxy in Table 4, and we confirm that all of them are statistically significant ($p < 10^{-4}$). This suggests that the disordered component of the B-field within the beam (i.e., small-scale B-fields) of observations at FIR wavelengths may have a larger contribution than at radio wavelengths.

In summary:

1. Spiral galaxies have a dominant ($\zeta > 0.8$), large-scale axisymmetric spiral B-field in both radio and FIR wavelengths.
2. Radio polarizations show larger ζ (more ordered B-fields) than those from FIR polarization measurements (more disordered B-fields). Specifically, the FIR B-fields have 2%–75% more disordered B-fields than those measured at radio wavelengths.

6. Discussion

One of the most striking results from this work are the differences in the patterns and angular dispersions between the FIR and radio B-fields shown in spiral and starburst galaxies. We will discuss these differences in terms of the intrinsic nature of the tracer and the B-field components, separating the large- and small-scale B-fields.

Magnetic fields extending over kiloparsec scales have been detected in many spiral galaxies using IR and radio polarimetric observations (Beck & Gaensler 2004; Beck 2015; Lopez-Rodriguez et al. 2022b). These B-fields are a fundamental part of galaxy evolution, driving gas mass inflows into the galactic core (Kim & Stone 2012), regulating the star formation rate through the removal of angular momentum in contracting protostellar gas clouds (Mouschovias & Ciolek 1999; Allen et al. 2003; Dapp & Basu 2010; Pattle et al. 2022), affecting the formation of molecular clouds (Abe & Inoue 2021; Tahani et al. 2022a, 2022b), and even potentially affecting the

global morphology and gas kinematics in disk galaxies (Battaner & Florido 2007; Ruiz-Granados et al. 2010; Martin-Alvarez et al. 2020; van de Voort et al. 2021). In spite of the substantial research efforts, the formation and structure of kiloparsec-scale B-fields in galaxies, as well as their possible role in the evolution of their hosts, are still outstanding questions in modern astrophysics.

The magnetic fields in spiral galaxies are observed to generally follow spiral patterns resembling the morphological spiral arms (Beck et al. 2019; Lopez-Rodriguez et al. 2020). This spatial correlation is in agreement with the current paradigm in which weak seed magnetic fields (Rees 1987; Subramanian 2016) are amplified by dynamo mechanisms such as small-scale ($<$50–100 pc) turbulence (Beck 1996; Haverkorn et al. 2008; Bhat et al. 2016; Brandenburg & Ntormousi 2022; Martin-Alvarez et al. 2022), and then are reorganized through differential galactic disk rotation and helical turbulence (large-scale dynamos; Gressel et al. 2008a, 2008b; Gent 2012; Bendre et al. 2015; Ntormousi et al. 2020).

While turbulent dynamos efficiently convert turbulent kinetic energy into magnetic energy (Widrow 2002; Kulsrud & Zweibel 2008; Federrath 2016; Rincon 2019), amplification takes place at the smallest scales and the resulting magnetic field follows the isotropic character of the driving turbulent field. The observations of kiloparsec-scale magnetic field structures in spiral galaxies (Beck et al. 2019; Lopez-Rodriguez et al. 2020; Borlaff et al. 2021) thus suggest that small-scale dynamos do not operate alone. Theoretical and modeling studies suggest that the efficient small-scale dynamos provide strong seed B-fields for other less efficient large-scale ordering mechanisms (i.e., differential rotation), which would subsequently align the field (Lou & Fan 1998; Arshakian et al. 2009; Bhat et al. 2016). In addition to differential rotation, the interaction between small-scale dynamos and spiral density waves has been proposed as a mechanism for ordering the magnetic field in spiral galaxies (Beck & Wielebinski 2013). Spiral density waves (Lin & Shu 1964; Bertin & Lin 1996; Sellwood 2011; Dobbs & Baba 2014; Font et al. 2019) periodically compress and shear the ISM, triggering star
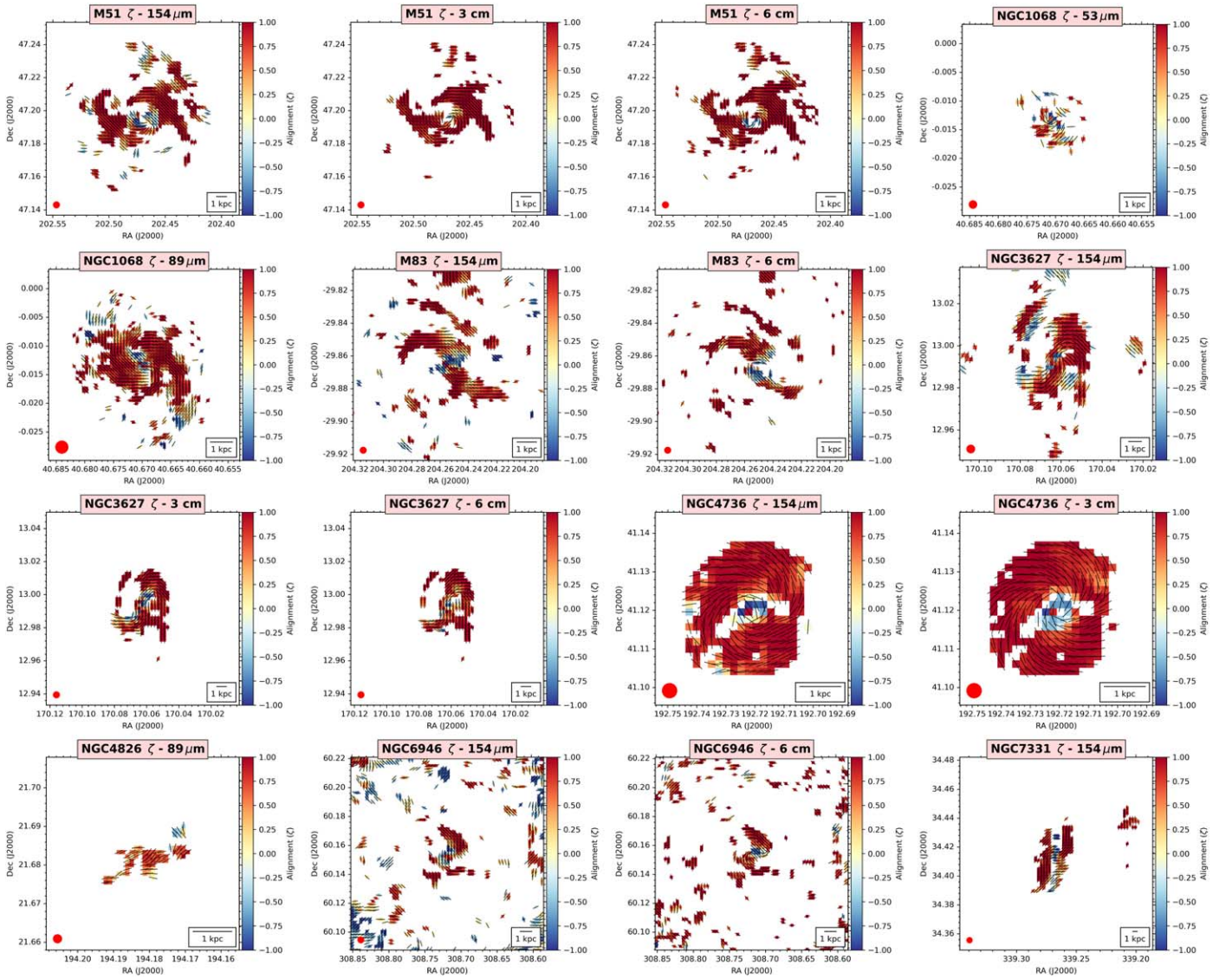
Figure 11. Disordered-to-ordered *B*-field ratio (magnetic alignment; ζ) maps at FIR and radio wavelengths of spiral galaxies. The measured (black dashes) *B*-field orientations are shown. Maps are shown with pixels at the Nyquist sampling (Table 1).

formation in their wake. Spiral density waves can also modulate parameters of the large-scale dynamo and lead to enhanced nonaxisymmetric fields (anti)correlated with the spiral (Mestel & Subramanian 1991; Shukurov 1998; Chamandy et al. 2013). As density waves travel through the ISM, magnetic field lines are sheared along the direction of the spiral arm, aligning the field with the morphological arms.

The mechanism described above to form kiloparsec-scale ordered galactic magnetic fields would work efficiently in grand-design spiral galaxies like M51 (Patrikeev et al. 2006) or M83 (Frick et al. 2016), where star formation takes place preferentially on the spiral arms. Flocculent spirals (i.e., NGC 253, NGC 6946) would be less affected by the spiral density arm shear compression, and as a consequence, they might present less ordered spiral magnetic fields, or lower alignment with their morphological counterparts (see NGC 6946). Similar results should apply to starburst galaxies (e.g., M82), while active galactic nucleus (AGN) dominated (e.g., Circinus), interacting, or recent merger galaxies (like the Antennae galaxies or Centaurus A; Chyży & Beck 2004;

Lopez-Rodriguez 2021; Lopez-Rodriguez et al. 2023) may, in addition, present shock or AGN-induced aligned magnetic fields (Lopez-Rodriguez et al. 2021b).

6.1. FIR versus Radio Magnetic Pitch Angles in Spiral Galaxies

We found that the orientation of the large-scale spiral *B*-fields traced through FIR polarimetric observations is statistically different from those measured through radio synchrotron polarization observations. Note that radio observations were convolved and rebinned to the angular resolution (13″6) of the HAWC+ observations. These results confirm the conclusions from Borlaff et al. (2021; SALSA I) in M51 and extend the results to a larger and more diverse sample of galaxies. A recent independent study on the same data sets used a linear decomposition of the polarization fields that also resulted in the same conclusions (Surgent et al. 2023). We showed that a large-scale ordered spiral *B*-field is the dominant *B*-field pattern for both radio and FIR wavelengths (with the exception of
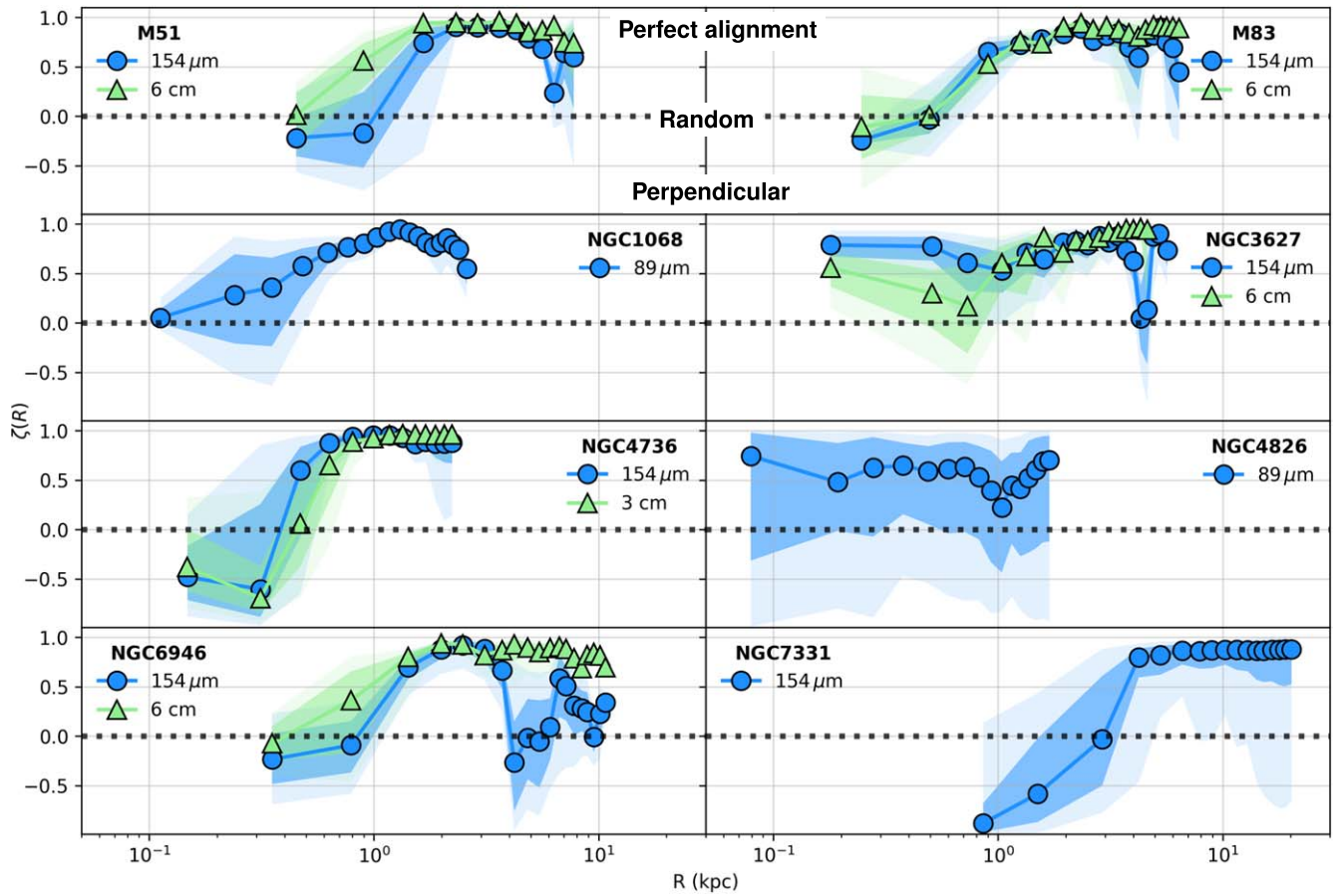
Figure 12. Radial profiles of the magnetic alignment parameter ζ of spiral galaxies at FIR (blue) and radio (green) wavelengths. $\zeta = +1$ corresponds to a perfect axisymmetric spiral alignment. $\zeta = 0$ corresponds to a completely random B-field. $\zeta = -1$ corresponds to a perpendicular alignment to the average B-field. The 68% (1σ) and 95% (2σ) statistical significance error contours are shown as shaded areas.

NGC 6946). However, the magnetic pitch-angle profiles traced with radio polarization observations present a more ordered distribution across the entire disk than those obtained with FIR (i.e., the outskirts of M51, M83, or the entire disk of NGC 6946). Specifically, the radio and FIR magnetic pitch angles show median angular dispersion of 8° and 18°, respectively, across the disks of spiral galaxies. In addition, the radio magnetic pitch angle is more open (i.e., larger pitch angles) with increasing galactocentric radius, while the FIR pitch angle tends to be wrapped tighter (i.e., smaller pitch angles) in the outskirts of spiral galaxies (with exception of M83).

Among the potential causes for these B-field morphological differences, we consider the intrinsic nature of the B-field tracer. FIR polarization observations trace the B-fields in the cold ($T_d = [19, 48]$ K) and dense ($\log_{10}(N_{\mathrm{HI+H2}}[\mathrm{cm}^{-2}]) = [19.9, 22.9]$) ISM (SALSA IV; Lopez-Rodriguez et al. 2022b). The measured FIR polarization is weighted by a combination of density, temperature, and grain alignment efficiency along the LOS and within the beam. Furthermore, the total FIR emission of galaxies has a typical vertical height of 0.10.6 kpc (Verstappen et al. 2013). Thus, the FIR B-fields are sensitive to the morphology and physical conditions of the dense ISM in the central few hundred parsecs of the galactic disk.

Radio synchrotron polarization traces the B-field in a volume-filling medium of the warm and diffuse ISM

(Beck et al. 2019). In spiral galaxies, the radio B-field morphology is observed to have a component parallel to the midplane of the disk and another component with an X-shaped structure extending several kiloparsecs above and below the disk (Hummel et al. 1988; Krause et al. 2020). Larger radio halos containing B-fields and cosmic rays (CRs) are found in galaxies with higher star formation rate surface densities (Wiegert et al. 2015). In addition, radio polarimetric observations suffer from Faraday rotation along the LOS. Radio B-fields are sensitive to the gradient of Faraday rotation (Sokoloff et al. 1998) and the physical conditions of both the halo and the galactic disk, but at 3 and 6 cm this effect is expected to be very small (less than $\pm5°$ rotation at 3 cm and less than $\pm20°$ at 6 cm; see Beck & Wielebinski 2013, Section 2.4). Beyond that limit, Faraday rotation systematic effects would greatly dominate the individual uncertainties of each beam, adding little information to our study. The main objective of the present work is to test observationally the structure of the magnetic field measured by different tracers (FIR vs. synchrotron). We attempt to do this by comparing data sets in the most compatible conditions (i.e., convolving the data sets of each galaxy to the largest beam size, applying quality cuts to both data sets, etc.). While it is certainly interesting to explore a wider range in the polarization spectra at optical and near-IR wavelengths, these wavelengths are strongly affected by dust/ electron scattering and have been shown to tell little about the

15
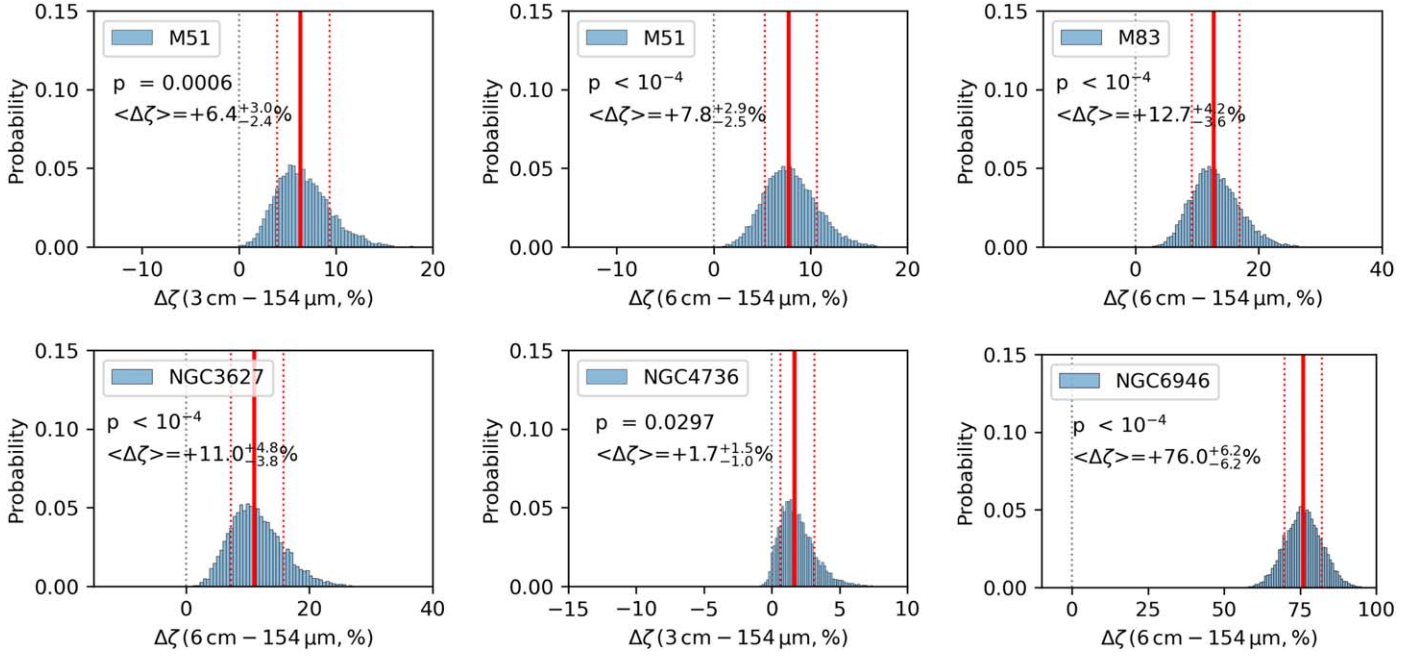
Figure 13. Difference between radio and FIR spiral magnetic alignment parameter ζ of spiral galaxies. The median difference $\Delta\zeta$ (solid red line) and 1σ uncertainty (dashed red line) for each histogram are shown in the top right of each panel (Table 4). The statistical p-value for the null hypothesis that $\Delta\zeta < 0$ is shown in the panel.

B-fields in external galaxies (e.g., Elvius 1972, 1978; Scarrott et al. 1991, 1993; Jones 2000; Pavel & Clemens 2012).

The large-scale dynamo (incorporating differential rotation) in galaxies can generate spiral B-fields over kiloparsec scales (Beck 1996; Gressel et al. 2008a, 2008b). This mechanism generates B-fields with similar pitch angles to those of the morphological spiral arms (Beck & Wielebinski 2013), although an offset between the B-fields and the spirals has been measured depending on the tracer (e.g., Beck et al. 2019). The large-scale dynamo could operate most efficiently in interarm regions because it may be suppressed or disturbed in the spiral arms (Beck 2015). The B-field associated with the dense (e.g., molecular) gas may respond in relatively short timescales to gravitational and kinematic effects like minor mergers, accretion of intergalactic material, and resonances. Diffuse atomic gas also responds collisionally, but its scale height is significantly higher, and its structure is more affected by supernova explosions and galaxy-scale processes, such as tidal interactions, bar, or spiral formation. Observational effects compatible with these hypotheses have been measured in several galaxies: in the outskirts of M51 (SALSA I; Borlaff et al. 2021), due to the interaction with M51b; in the central starburst of NGC 1097 (SALSA II; Lopez-Rodriguez et al. 2021a), where the radio B-field has a spiral shape following the diffuse gas and the FIR B-field is cospatial with a galactic shock at the boundaries of the bar and the starburst ring; and, finally, in the relic spiral arm of the Antennae galaxies (SALSA VI; Lopez-Rodriguez et al. 2023), where the radio B-field is radial and cospatial with the H I gas dynamics and the FIR B-field is spiral and cospatial with the dense and molecular ISM.

We suggest that the differences of the radial magnetic pitch angles at radio and FIR wavelengths may be caused by the "averaging" of the several components of the B-fields along the LOS owing to the different nature of the two tracers. Due to the relatively narrow extension of the molecular disk above and below the galactic plane compared to more diffuse components of the ISM, the FIR magnetic pitch angle efficiently traces the B-field in the midplane of the galaxy (Figure 10). Angular variations of the FIR magnetic pitch angle are driven by the dense ISM and star-forming regions (Section 6.2). However, the radio magnetic pitch angle may be more sensitive to the extraplanar B-field as the distance from the core increases. This may occur by the combination of (a) an increase of the vertical height of the X-shaped B-field above and below the disk as galactocentric distance increases, (b) an increase of the polarized flux from the X-shaped structure rather than from the disk, and/or (c) depolarization in the arms due to an increase of random turbulent B-fields.

We conclude that the FIR and radio magnetic pitch angles may trace similar B-fields in the midplane of the disk within the central few kiloparsecs of spiral galaxies. However, the radio pitch angle may be arising from different vertical heights as galactocentric radius increases. Specifically, the radio B-field may be extraplanar above the disk along the LOS, while the FIR is colocated with the midplane of the disk at large galactocentric radii.

6.2. Ratio of Disordered to Ordered B-fields at FIR and Radio

We have introduced the magnetic alignment parameter ζ as a proxy of the disordered-to-ordered B-field ratio on a pixel-to-pixel basis (see Section 5.1). The analysis of the ζ alignment maps allowed us to compare the disordered-to-ordered B-field ratio difference between FIR and radio polarimetric observations. Our results indicate that spiral galaxies have a dominant large-scale B-field with a $\zeta > 0.8$ across their disk. We found that the FIR B-field is 2%–75% more disordered than the radio B-field across the galaxy disk.

Individual measurements with $\zeta \neq 1$ indicate that angular dispersion may be due to (a) B-field variations below the physical scale of the beam of the observations and/or (b) B-field variations from some physical mechanisms larger than the physical scale of the beam of the observations. For the latter, systematic angular dispersions across several beams are expected, while random angular dispersion between beams can indicate the signature of small-scale B-fields. The azimuthally averaged ζ radial profiles, $\zeta(R)$, allow us to identify the variation of the disordered to ordered magnetic field in the spiral galaxies of our sample. Variations of $\zeta(R)$ indicate deviations from the axisymmetric large-scale ordered B-field at scales larger than the beam of the observations. Angular variations larger than the beams of our observations can be driven by tangled random B-fields, B-field instabilities (Parker loops), and/or gas dynamics due to winds, outflows, supernovae, galaxy dynamics, or galaxy interactions. Angular variations smaller than the beam of our observations can also be driven by tangled random B-fields owing to star formation, supernovae, or the increase of gas turbulence due to galaxy interaction or gas dynamics.

Lopez-Rodriguez et al. (2022b; SALSA IV) analyzed the trends of the FIR polarization fraction with the column density as a proxy to estimate the random B-fields in the ISM. SALSA IV showed that the spiral galaxies have a relative increase of isotropic random FIR B-fields driven by star-forming regions in the spiral arms. In Section 6.1 we showed that the FIR and radio polarized emissions trace different components of the B-field in the disk of galaxies. In addition, $\Delta\zeta$ showed that the FIR B-field is 2%–75% more disordered than the radio B-field as measured by the independent measurements of ζ. These results suggest that the B-field observations associated with dense, dusty, star-forming regions are less ordered than warmer, less dense regions of the ISM.

FIR observations of molecular clouds in the Milky Way showed that the B-field orientation can be drastically different as a function of the density of the ISM (Pillai et al. 2020). It is possible, then, that observationally the properties of both the small- and large-scale magnetic fields differ as a function of the tracer and the phases of the ISM. This has been suggested by Seta & Federrath (2022) using MHD turbulent boxes with a multiphase ISM. These authors measured that the "cold" ($T < 10^3$ K) phase is more tangled than the "warm" ($T \geqslant 10^3$ K) phase.

Our results indicate that the FIR polarimetric observations can be used as an indicator of the small-scale B-fields associated with the activity of the star-forming regions and the morphology of the molecular clouds within a vertical height of a few hundred parsecs in the disks of spiral galaxies. In addition, $\zeta(R)$ also shows that the FIR B-fields have larger fluctuation across the disk than radio B-fields. This result may indicate that FIR polarization is more sensitive to large-scale mechanisms (i.e., outflows, Parker loops, galaxy interaction) affecting the galaxy.

6.3. Starburst Galaxies

The differences between the magnetic field traced by FIR and radio polarimetric observations are even more striking in our subsample of starburst galaxies (M82, NGC 253, and NGC 2146). We found that FIR polarimetric observations are able to trace the B-field by means of magnetically aligned dust grains along the galactic outflows within the 53–214 μm wavelength range.

For M82, we estimate a large change of the average magnetic field position angle ($\langle PA_B^{hist} \rangle$ and $\langle PA_B^{int} \rangle$) with wavelength in both FIR (from $\sim 150°$ in 53 μm to $\sim 60°$ in 214 μm) and radio ($\sim 90°$ in 6 cm; see Figure 8 and Table 5). The radio polarimetric observations trace the B-field by means of synchrotron emission in a magnetized bar mostly coincident with the galactic disk (Adebahr et al. 2013, 2017). A similar conclusion can be obtained from the observations of NGC 253 (Heesen et al. 2011). While the inner regions show B-field orientations parallel to the disk of the galaxy in all wavelengths, strong discrepancies are observed in the outskirts, which might be a signature of galactic outflows. Although some Faraday depolarization may be affecting the radio polarimetric observations, we suggest that the discrepancy may be produced by the limited lifetime of the CRs along the galactic outflows. This may be explained by the weak total synchrotron emission in the outflow (Adebahr et al. 2013; Figure 6). In addition, the steep spectral indexes may be an indication of rapid aging of the CR electrons. FIR total intensity observations with Herschel have shown ~ 10 kpc scale extensions of dust above and below the disk (Roussel et al. 2010). The galactic outflow may have expelled $\geqslant 25\%$ of the total dust mass of the galaxy (Roussel et al. 2010), making the cold phase of the ISM the bulk of the mass along the galactic outflow. Thus, the B-fields along the galactic outflows of starburst galaxies are better traced by using FIR polarimetric observations.

Radio polarimetric observations have measured an X-shaped structure extending several kiloparsecs above the disks of edge-on spiral galaxies (Krause et al. 2020). This vertical B-field is different from that observed here in starburst galaxies. Our FIR polarimetric observations in edge-on galaxies do not show signs of an X-shaped B-field structure. This is expected, as the vertical height of dust emission is 0.1–0.6 kpc (Verstappen et al. 2013), while the X-shaped B-field observed in radio corresponds to synchrotron polarized emission from warm gas in the halo at several kiloparsec scales.

FIR polarimetric observations also reveal large structural differences of the B-field with wavelength in the 53–214 μm range, as observed in Circinus (Figure 3) and NGC 2146 (Figure 6). For Circinus, the 53 and 89 μm B-fields may be dominated by the starburst ring and the inner bar, while the 214 μm B-field may be tracing the B-field in the outer bar and spiral arms of the host galaxy (Maiolino et al. 2000; Izumi et al. 2018). Further modeling is required to quantify these results.

The most extreme case is NGC 2146. This galaxy shows a B-field with an orientation perpendicular to the galactic disk in the 53–89 μm wavelength range associated with the galactic outflow. The 214 μm observations reveal a parallel B-field to the galactic disk associated with the galactic B-field. Lopez-Rodriguez et al. (2022b; SALSA IV) computed the polarized spectral energy distribution of starburst galaxies showing a minimum within the 89–154 μm wavelength range. The falling 53–154 μm polarized spectrum was suggested to be produced by a decrease in the dust grain alignment efficiency due to a gradient of dust temperatures along the LOS. The rise spectrum at 154–214 μm was suggested to be produced by the dust becoming more optically thin at larger wavelengths. Thus, the measured 154 μm B-field orientation is expected to be the

transition between the two regimes (see Section 3.2.1). In addition, the extremely complex morphological structure of NGC 2146 suggests that it is the remnant of a recent interaction that triggered star formation bursts (Martini et al. 2003; Tarchi et al. 2004; Erwin 2005). While it is beyond the scope of this paper to explore this, the *B*-field orientation differences detected within the different SOFIA HAWC+ bands suggest that FIR polarized emission could be dominated by different populations of dust grains as a function of wavelength, revealing different physical regimes in terms of density, radiation, or turbulence.

7. Conclusions

The HAWC+/FIR polarimetric observations of the SALSA Legacy Program of 14 nearby (<20 Mpc) galaxies analyzed in this paper and presented in the previous publications from the project (SALSA I–IV, VI) provide a previously unexplored view of a fundamental factor in galaxy evolution: the *B*-fields in the dense and cold ISM of galaxies. While extragalactic *B*-fields have been observed for decades in radio polarization observations (e.g., Beck et al. 2019), high spatial resolution FIR polarimetric maps from molecular clouds in the Milky Way (e.g., Pillai et al. 2020) have demonstrated that the structure of magnetic fields is a strong function of the density of the ISM at scales of hundreds of parsecs.

Here we provide quantitative evidence that the kiloparsec scale of galactic magnetic fields depends strongly on the tracer: radio polarization observations of the synchrotron emission at 3 and 6 cm, and FIR polarization observations of the thermal polarized emission from magnetically aligned dust grains. In addition, we introduce the alignment parameter ζ (Section 5) as a quantitative measurement of the dispersion between the measured *B*-field orientation and a large-scale axisymmetric spiral magnetic field. ζ allows us to estimate how well ordered a spiral magnetic field is and to compare it as a function of different observational tracers.

Our results suggest that radio and FIR polarization observations do not necessarily trace the same magnetic field structures. For most of our galaxies, significant differences are found in terms of local and global orientation of the magnetic field (Section 3.2), the pitch angle of spiral galaxies (Section 4), and the dispersion of the magnetic spiral structure (Section 5.2). We find evidence that even FIR polarization observations can trace different structures of the magnetic field as a function of wavelength as observed in NGC 2146 (53–214 μm; see Figure 6). The differences in the magnetic pitch-angle profiles (Figure 10) and the alignment ζ profiles (Figure 12) indicate that radio polarization observations tend to trace a more regular and stable structure of the magnetic field, with less variation of the magnetic pitch angle and a higher level of alignment ζ. The five spiral galaxies studied with available FIR and radio polarization observations presented a statistically higher magnetic field dispersion in FIR than in radio (see Figure 13).

While our observations are limited by spatial resolution and thus not able to resolve individual molecular clouds, all results point toward the conclusion that FIR polarization observations trace a less ordered structure of the magnetic field than radio polarization observations. We suggest that FIR polarization observations are dominated by the emission from magnetically aligned dust grains cospatial with the cold, dense ISM, while radio polarization observations trace more diffuse regions of

the ISM, less dominated by kinematic turbulence. Each beam from both radio and FIR polarization maps would be tracing an average of the magnetic field inside them, but dominated by the dense, dusty molecular clouds in FIR. Star formation, outflows, accretion, and the morphological complexity of the galactic filaments of dust would increase the dispersion of the magnetic field from the average kiloparsec-scale magnetic field orientation, with a lower effect on less dense phases of the ISM.

High-resolution, FIR polarization observations of galaxies such as those provided by SOFIA/HAWC+ until its last flight in 2022 September are vital to understand the role of magnetic fields in the evolution of the universe. While facilities like ALMA, South Pole Telescope, or James Clerk Maxwell Telescope provide polarimetric observations in submillimetric and/or FIR wavelength ranges, they lack the sensitivity and/or spatial resolution in the required wavelengths to achieve the same scientific requirements in nearby galaxies. In the absence of facilities such as SOFIA, unique in their ability to investigate the dusty components of galaxies and their magnetic fields, the astronomical community has no current alternatives to explore the magnetic fields inside the dust components of nearby galaxies through FIR polarimetry. Only the support of the astronomical community through proposed missions like PRIMA (Bradford et al. 2022, potential launch no earlier than 2030) for the upcoming NASA FIR Probe missions or future FIR polarimetric missions will ensure a continuation of this field in the next decades.

those of the authors and should not be interpreted as representing the official policies, either expressed or implied, of the National Aeronautics and Space Administration (NASA) or the U.S. Government. The U.S. Government is authorized to reproduce and distribute reprints for Government purposes notwithstanding any copyright notation herein.

The authors thank the careful revision and useful comments from the anonymous referee, who contributed to greatly improving this manuscript. The authors thank Dr. Yik Ki Ma from the Research School of Astronomy & Astrophysics of the Australian National University in Canberra, Australia for his careful revision of the manuscript.

Facilities: SOFIA (HAWC+), ALMA, Herschel, VLA.

Software: ASTROPY (Astropy Collaboration et al. 2013), APLPY (Robitaille & Bressert 2012), MATPLOTLIB (Hunter 2007),

Appendix A
Measurements of the Polarization Angles at FIR and Radio Wavelengths

This appendix shows the histograms of the *B*-field orientations at 3 and 6 cm, which are shown in Figure 14. Table 5 shows the circular average and integrated polarization fraction and *B*-field orientation of the galaxies included in the SALSA sample. Table 6 shows the noise levels obtained and the quality cuts applied to each data set.
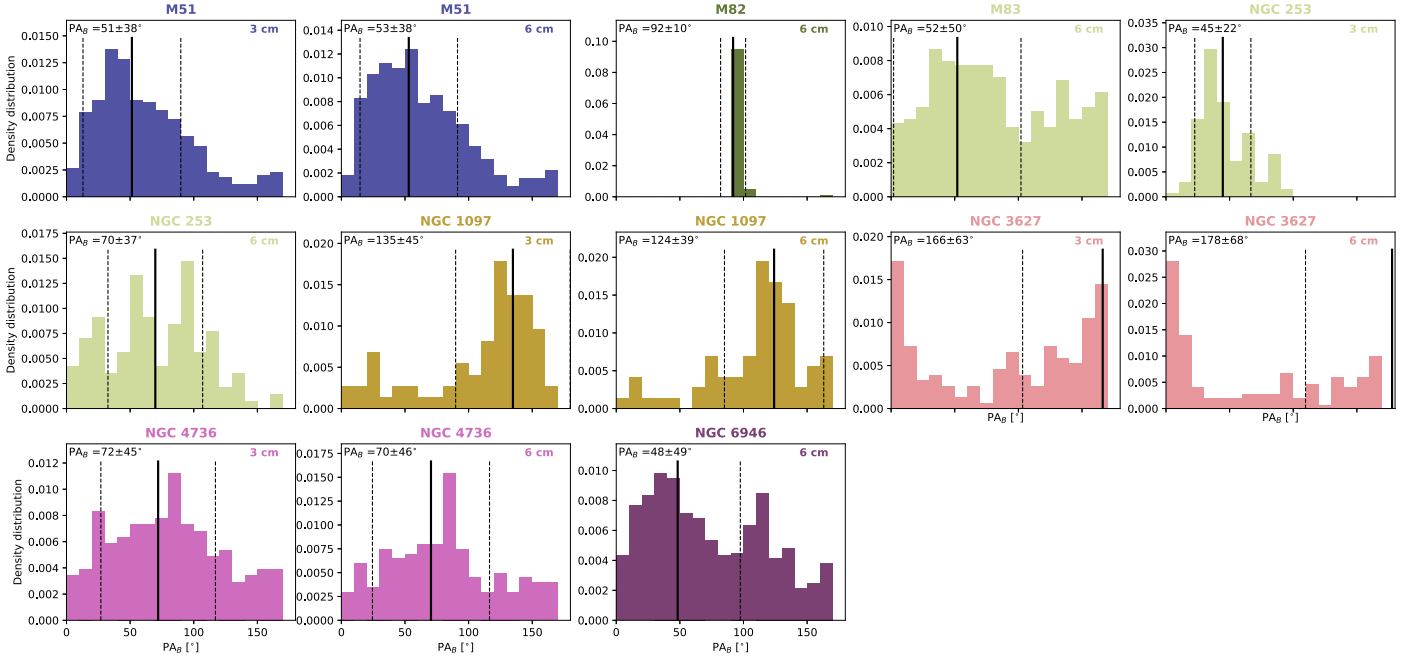
Figure 14. Histograms of the *B*-field orientations for the galaxies with radio polarimetric observations (Table 2). The histograms are set to 10° bins, each galaxy is shown in a unique color, and the median (black solid line) and 1σ uncertainty (black dashed line) for the radio observations are shown. Given the similarities of the *B*-field orientations between 3 and 6 cm wavelengths, only the histograms of the *B*-field orientations at 6 cm are shown in Figure 8.

Table 5
Median and Integrated Polarization Fraction and *B*-field Orientation of Galaxies

Galaxy	Band (μm)	$\langle \mathrm{PA}_{B,\mathrm{FIR}}^{\mathrm{hist}} \rangle$ (deg)	$\langle \mathrm{PA}_{B,\mathrm{FIR}}^{\mathrm{int}} \rangle$ (deg)	Band (cm)	$\langle \mathrm{PA}_{B,\mathrm{Radio}}^{\mathrm{hist}} \rangle$ (deg)	$\langle \mathrm{PA}_{B,\mathrm{Radio}}^{\mathrm{int}} \rangle$ (deg)
(1)	(2)	(3)	(4)	(5)	(6)	(7)
Centaurus A	89	124 ± 28	126 ± 9	...	...	...
Circinus	53	52 ± 23	59 ± 13	...	...	...
	89	28 ± 37	30 ± 12	...	...	...
	214	1 ± 77	179 ± 2	...	...	...
M51	154	51 ± 36	56 ± 12	3	51 ± 38	47 ± 1
				6	53 ± 38	53 ± 1
M82	53	156 ± 52	155 ± 4	6	92 ± 10	...[a]
	89	154 ± 55	153 ± 5	...	...	...
	154	83 ± 43	86 ± 7	...	...	...
	214	58 ± 41	53 ± 3	...	...	...
M83	154	59 ± 40	50 ± 10	6	52 ± 50	44 ± 1
NGC 253	89	50 ± 41	39 ± 19	3	45 ± 22	44 ± 2
	154	62 ± 23	164 ± 56	6	70 ± 26	70 ± 3
NGC 1068	53	124 ± 49	39 ± 84	...	...	...
	89	139 ± 48	135 ± 10	...	...	...
NGC 1097	89	131 ± 32	132 ± 5	3	135 ± 45	134 ± 1
	154	126 ± 35	134 ± 16	6	124 ± 39	128 ± 1
NGC 2146	53	64 ± 16	65 ± 10	...	...	...
	89	74 ± 29	80 ± 9	...	...	...
	154	165 ± 61	160 ± 9	...	...	...
	214	120 ± 20	119 ± 4	...	...	...
NGC 3627	154	177 ± 60	17 ± 19	3	166 ± 63	174 ± 1
				6	178 ± 68	0 ± 1
NGC 4736	154	85 ± 42	88 ± 7	3	72 ± 45	72 ± 1
				6	70 ± 46	71 ± 1
NGC 4826	89	106 ± 31	104 ± 10	...	...	...
NGC 6946	154	151 ± 55	161 ± 11	6	48 ± 49	47 ± 1
NGC 7331	154	127 ± 30	121 ± 6	...	...	...

Notes. Column (1): galaxy name. Column (2): central wavelength of the HAWC+ band. Column (3): median polarization angle based on individual measurements at FIR wavelengths. Column (4): median polarization angle based on the integrated Stokes *IQU* of the full galaxy at FIR wavelengths. Column (5): central wavelength of the band at radio wavelengths. Column (6): median polarization angle based on individual measurements at radio wavelengths. Column (7): median polarization angle based on the integrated Stokes *IQU* of the full galaxy at radio wavelengths.
[a] Stokes *QU* were not available.

Table 6
Noise Level in Total Intensity (*I*) and Polarized Intensity (PI) and Quality Cuts of the FIR and Radio Polarization Observations of the Galaxies in the Sample

Galaxy	Band (μm)	$\sigma_I^{\rm FIR}$ (Jy arcsec^{-2})	$\sigma_{\rm PI}^{\rm FIR}$ (Jy arcsec^{-2})	Band (cm)	$\sigma_I^{\rm Radio}$ (Jy arcsec^{-2})	$\sigma_{\rm PI}^{\rm Radio}$ (Jy arcsec^{-2})	S/N$_{\rm FIR,\,PI}$	$p_{\rm lim}$ (%)	S/N$_{\rm FIR,\,I}$
(1)	(2)	(3)	(4)	(5)	(6)	(7)	(8)	(9)	(10)
Centaurus A	89	1.39×10^{-4}	3.39×10^{-3}	...	...	...	2.5	20	10
Circinus	53	9.17×10^{-4}	10^{-2}	...	...	...	2.3	20	10
	89	1.22×10^{-4}	2.96×10^{-3}	...	...	...	3.0	20	10
	214	3.72×10^{-5}	4.74×10^{-3}	...	...	...	2.5	20	10
M51	154	2.23×10^{-5}	1.52×10^{-3}	3	1.75×10^{-7}	2.32×10^{-7}	3.0	20	10
				6	2.16×10^{-7}	2.28×10^{-7}			
M82	53	6.27×10^{-4}	6.84×10^{-3}	6	[a]	[a]	3.0	20	80
	89	1.65×10^{-4}	4.02×10^{-3}	...	...	...	3.0	20	80
	154	3.57×10^{-5}	2.46×10^{-3}	...	...	...	3.0	20	20
	214	3.96×10^{-5}	5.0×10^{-3}	...	...	...	3.0	20	20
M83	154	2.57×10^{-5}	1.78×10^{-3}	6	2.2×10^{-7}	2.5×10^{-7}	2.5	20	10
NGC 253	89	2.80×10^{-4}	6.52×10^{-3}	3	4.10×10^{-7}	4.63×10^{-7}	2.5	10	20
	154	3.30×10^{-4}	2.12×10^{-2}	6	7.88×10^{-7}	6.13×10^{-7}	2.0	10	20
NGC 1068	53	6.32×10^{-4}	7.00×10^{-3}	...	...	...	2.0	10	10
	89	2.60×10^{-4}	1.18×10^{-3}	...	...	...	2.0	10	10
NGC 1097	89	2.16×10^{-4}	4.98×10^{-3}	3	4.65×10^{-8}	1.47×10^{-7}	3.0	10	10
	154	1.47×10^{-4}	9.88×10^{-3}	6	5.41×10^{-8}	2.00×10^{-7}	2.0	10	10
NGC 2146	53	4.03×10^{-4}	4.39×10^{-3}	...	...	...	3.0	20	30
	89	1.39×10^{-4}	3.38×10^{-3}	...	...	...	3.0	20	20
	154	3.27×10^{-5}	2.25×10^{-3}	...	...	...	3.0	20	20
	214	2.24×10^{-5}	2.85×10^{-3}	...	...	...	3.0	20	20
NGC 3627	154	2.59×10^{-5}	1.79×10^{-3}	3	4.33×10^{-7}	5.10×10^{-8}	2.0	20	40
				6	1.13×10^{-6}	8.51×10^{-8}			
NGC 4736	154	4.74×10^{-5}	3.22×10^{-3}	3	6.32×10^{-8}	6.94×10^{-8}	2.0	20	68
				6	2.05×10^{-8}	4.76×10^{-8}			
NGC 4826	89	1.82×10^{-4}	4.42×10^{-3}	...	...	...	2.3	20	20
NGC 6946	154	3.10×10^{-5}	2.14×10^{-3}	6	9.02×10^{-9}	5.94×10^{-8}	2.3	20	20
NGC 7331	154	2.19×10^{-5}	1.50×10^{-3}	...	...	...	2.8	20	45

Notes. Column (1): galaxy name. Column (2): central wavelength of the HAWC+ band. Column (3): total intensity noise level in FIR. Column (4): polarized intensity noise level in FIR. Column (5): central wavelength of the band at radio wavelengths. Column (6): total intensity noise level in radio. Column (7): polarized intensity noise level in radio. Column (8): limiting S/N in polarization intensity. Column (9): limiting polarization fraction. Column (10): limiting S/N in total intensity. The polarization fraction limit of $P = 20\%$ is given by the maximum polarization fraction ($p_{\rm max} = 19.8\%$) of dust measured by Planck observations (Planck Collaboration et al. 2015). Note that more stringent quality cuts were applied to some specific galaxies, to avoid systematic effects. For more specific information about the quality cuts chosen for each galaxy we refer to Lopez-Rodriguez et al. (2021b).
[a] Stokes *QU* were not available.

Appendix B
Measuring the Pitch Angle of the FIR and Radio Polarization Fields

We analyze the magnetic pitch angles of the *B*-field maps following the methodology (Mohawc) presented by Borlaff et al. (2021) on M51. Here we summarize the steps to estimate the magnetic pitch angle, Ψ_B, as a function of the galactocentric radius of spiral galaxies. Mohawc uses the Stokes *IQU* maps to derive the Ψ_B profiles on a pixel-by-pixel basis, assuming that all the *B*-field orientations are on the galactic plane viewed at a certain inclination, *i*, with respect to the observer and position angle, θ, on the plane of the sky. The uncertainties of the Stokes *IQU*, position angle, and inclination are taken into account through Monte Carlo simulations. Our magnetic pitch-angle estimation method entails processing the data on a pixel-by-pixel basis, allowing the user to separate different regions of the galaxy by using masks (if desired). The steps followed by Mohawc can be summarized as follows:

1. The debiased polarization degree and its associated uncertainty are computed using the Stokes *IQU*

parameters and their uncertainties δI, δQ, δU:

$$P_{\rm debias} = \sqrt{P^2 - \delta P^2}, \qquad (B1)$$

following Serkowski (1974), where

$$P = \sqrt{\left(\frac{Q}{I}\right)^2 + \left(\frac{U}{I}\right)^2} \qquad (B2)$$

and

$$\delta P = \frac{1}{I}\sqrt{\frac{(Q \times \delta Q)^2 + (U \times \delta U)^2}{Q^2 + U^2} + \delta I^2 \frac{Q^2 + U^2}{I^2}}. \qquad (B3)$$

2. The *B*-field orientations are then reprojected to a new reference frame where the galaxy is observed face-on, using coordinates of the galactic center (α, δ), the galactic disk inclination *i*, and tilt angle θ. The morphological parameters for each galaxy are summarized in Table 3.

3. An azimuthal angular mask is created. The azimuthal mask is generated such that the deprojected *B*-field orientation at each pixel location is perpendicular to the radial direction. We will refer to this idealized field as the *zero pitch-angle* field or Ξ.

4. The magnetic pitch angle at each pixel, $\Psi_B(x, y)$, is calculated as the difference between the measured PAs of the B-field orientation and the Ξ vector field.

5. The magnetic pitch-angle profile $\Psi_B(x, y)$ is then averaged at each radius from the core. The radial bins are linearly spaced, and their number is optimized as a compromise between signal-to-noise ratio (S/N) and spatial resolution. The angular average as a function of the galactocentric radius, R, is performed as follows:

$$\overline{\Psi_B}(R) = \text{atan2}\left(\frac{\langle \cos \Psi_B(x, y) \rangle}{\langle \sin \Psi_B(x, y) \rangle} \right), \tag{B4}$$

where the $\langle \rangle$ operator indicates a robust median value (based on randomized Monte Carlo simulations) and $\overline{\Psi_B}(R)$ is the averaged magnetic pitch-angle value for a certain radial bin.

For each galaxy, the process detailed above is repeated 10,000 times, using Monte Carlo simulations to include the uncertainties of the tilt angle, the inclination, and the Stokes parameters. We assume that each parameter follows a Gaussian probability distribution, with a standard deviation σ equal to their uncertainties. We use the probability distribution for the pitch angle of each pixel to calculate the median magnetic pitch angle, $\overline{\Psi_B}$ radial profiles, and their uncertainties (68%, 95%, equivalent to 1σ, 2σ). For all the analyses, we consider a critical level of at least $p = 0.05$ (95%) to declare statistical significance.

Note that one of the limitations of Mohawc resides in the estimation of the pitch angle within the central two to three beams at the core of the galaxies. This limitation is due to the small number of measurements per annulus to obtain statistically significant measurements of the pitch angles (see Figure 22 by Borlaff et al. 2021). Our analysis only takes into account the polarization measurements in the galaxy disks after two beams (4 pixels in diameter) from the core. Systematic errors are expected owing to the lack of statistics in regions too close to the center, or affected by internal core phenomena, like rings, bars, or AGNs. NGC 1068, M83, and M51 are examples of extreme values on their innermost bins, due to statistics, presenting more acceptable values in the second bin.

Appendix C
Line Integral Convolution (LIC) RGB Background Components

In this appendix we summarize the components used as the RGB backgrounds in Figure 1. Note that this figure is only for illustrative purposes, and no analyses were derived from these data sets:

1. *M51*: Hubble/ACS, F658N (Hα) and F814W (red), F555W (green), and F435W (blue)—NASA/ESA S. Beckwith (STScI) and the Hubble Heritage Team (STScI/AURA).

2. *M82*: The image combines visible starlight (gray) and Hα emission (red) from the Kitt Peak 2.1 m (Spitzer Infrared Nearby Galaxy Survey Legacy project) and near-infrared and mid-infrared starlight plus dust from Spitzer IRAC and SOFIA (3.6 and 53 μm; yellow; credit: J. Moustakas et al.).

3. *M83*: Spitzer/IRAC 3.6 μm (blue), 4.5 μm (green), 8 μm (red) (NASA/JPL-Caltech).

4. *NGC 253*: MPG/ESO 2.2 m telescope Wide Field Imager (WFI, R, V, Hα and O III composition)—La Silla Observatory (Credit: ESO).

5. *NGC 1068*: SDSS RGB image, combined with hard X-ray (magenta, NASA/NuSTAR). Credit: NASA/JPL-Caltech/Roma Tre Univ.

6. *NGC 1097*: VLT/NACO J (blue), H (green), and K_s band (red). Credit: ESO/Prieto et al.

7. *NGC 2146*: Hubble/ACS: F814W (blue), F658N (red), F814W + F658N (green). Credit: ESA/Hubble & NASA.

8. *NGC 3627*: Spitzer/IRAC 3.6 μm (blue), 4.5 μm (green), 8 μm (red). Credit: NASA/JPL-Caltech/R. Kennicutt (University of Arizona) and the SINGS Team.

9. *NGC 4736*: Hubble/WFPC2: F450W (blue), F555W (green), F814W (orange), F336W (red). Credit: ESA/Hubble & NASA.

10. *NGC 4826*: Hubble/WFC3: F336W (purple), F438W (blue), F555W (green), F814W (orange), F275W (red). Credit: ESA/Hubble & NASA, J. Lee and the PHANGS-HST Team. Acknowledgment: Judy Schmidt.

11. *NGC 6946*: Spitzer/IRAC 3.6 μm (blue), 4.5 μm (green), 8 μm (red) (NASA/JPL-Caltech). Credit: NASA/JPL-Caltech L.Proudfit.

12. *NGC 7331*: LRGB color-composite CCD image taken with the 32-inch Schulman Telescope at Mt. Lemmon. Credit: Adam Block/Mount Lemmon SkyCenter/University of Arizona.

13. *Antennae*: Hubble/ACS and WFC3: F336W (blue), F435W (blue), F550M (cyan), F555W (cyan), F625W (green), F814W (orange), F658N (red). Credit: ESA/Hubble & NASA.

14. *Centaurus A*: MPG/ESO 2.2 m telescope WFI (B—blue; V—green), Atacama Pathfinder Experiment LABOCA (870 μm—orange), Chandra X-ray Observatory (blue). Credit: ESO/WFI (Optical); MPIfR/ESO/APEX/A. Weiss et al. (Submillimetre); NASA/CXC/CfA/R. Kraft et al. (X-ray).

15. *Circinus*: Hubble/WFPC2: F502N (blue), F547N (green), F814W (yellow), F656N (red). Credits: Andrew S. Wilson (University of Maryland); Patrick L. Shopbell (Caltech); Chris Simpson (Subaru Telescope); Thaisa Storchi-Bergmann and F. K. B. Barbosa (UFRGS, Brazil); and Martin J. Ward (University of Leicester, UK) and NASA/ESA.

ORCID iDs

Alejandro S. Borlaff ◉ https://orcid.org/0000-0003-3249-4431
Enrique Lopez-Rodriguez ◉ https://orcid.org/0000-0001-5357-6538
Susan E. Clark ◉ https://orcid.org/0000-0002-7633-3376
Evangelia Ntormousi ◉ https://orcid.org/0000-0002-4324-0034
Konstantinos Tassis ◉ https://orcid.org/0000-0002-8831-2038
Sergio Martin-Alvarez ◉ https://orcid.org/0000-0002-4059-9850
Mehrnoosh Tahani ◉ https://orcid.org/0000-0001-8749-1436
Daniel A. Dale ◉ https://orcid.org/0000-0002-5782-9093

Ignacio del Moral-Castro ⓘ https://orcid.org/0000-0001-8931-1152
Julia Roman-Duval ⓘ https://orcid.org/0000-0001-6326-7069
John E. Beckman ⓘ https://orcid.org/0000-0001-5747-7086
Sarah Eftekharzadeh ⓘ https://orcid.org/0000-0002-8281-8388

References

Abe, D., Inoue, T., Inutsuka, S.-i., & Matsumoto, T. 2021, ApJ, 916, 83
Adebahr, B., Krause, M., Klein, U., et al. 2013, A&A, 555, A23
Adebahr, B., Krause, M., Klein, U., Heald, G., & Dettmar, R. J. 2017, A&A, 608, A29
Allen, A., Li, Z.-Y., & Shu, F. H. 2003, ApJ, 599, 363
Arshakian, T. G., Beck, R., Krause, M., & Sokoloff, D. 2009, A&A, 494, 21
Astropy Collaboration, Robitaille, T. P., Tollerud, E. J., et al. 2013, A&A, 558, A33
Battaner, E., & Florido, E. 2007, Frontiers in Astronomy and Space Sciences, 328, 92
Beck, R. 1991, A&A, 251, 15
Beck, R. 1996, NAWG II, 1996, 262
Beck, R. 2007, A&A, 470, 539
Beck, R. 2015, A&ARv, 24, 4
Beck, R., Chamandy, L., Elson, E., & Blackman, E. G. 2019, Galax, 8, 4
Beck, R., Fletcher, A., Shukurov, A., et al. 2005, A&A, 444, 739
Beck, R., & Gaensler, B. M. 2004, NewA, 48, 1289
Beck, R., & Wielebinski, R. 2013, in Planets, Stars and Stellar Systems, ed. T. D. Oswalt & G. Gilmore, Vol. 5 (Cham: Springer), 641
Bendre, A., Gressel, O., & Elstner, D. 2015, Frontiers in Astronomy and Space Sciences, 336, 991
Bertin, G., & Lin, C. C. 1996, Spiral Structure in Galaxies a Density wave Theory (Cambridge, MA: MIT Press)
Bhat, P., Subramanian, K., & Brandenburg, A. 2016, MNRAS, 461, 240
Bland-Hawthorn, J., Gallimore, J. F., Tacconi, L. J., et al. 1997, Ap&SS, 248, 9
Borlaff, A. S., Lopez-Rodriguez, E., Beck, R., et al. 2021, ApJ, 921, 128
Bradford, C., Glenn, J., Armus, L., et al. 2022, AAS Meeting, 54, 304.07
Brandenburg, A., & Ntormousi, E. 2022, arXiv:2211.03476
Brandenburg, A., & Subramanian, K. 2005, PhR, 417, 1
Braun, R., Walterbos, R. A. M., Kennicutt, R. C. J., & Tacconi, L. J. 1994, ApJ, 420, 558
Brinks, E., Skillman, E. D., Terlevich, R. J., & Terlevich, E. 1997, Ap&SS, 248, 23
Cabral, B., & Leedom, L. C. 1993, in Proc. of the 20th Annual Conf. on Computer Graphics and Interactive Techniques, SIGGRAPH '93 (New York: Association for Computing Machinery), 263
Chamandy, L., Subramanian, K., & Shukurov, A. 2013, MNRAS, 428, 3569
Chyży, K. T., & Beck, R. 2004, A&A, 417, 541
Chyży, K. T., & Buta, R. J. 2008, ApJL, 677, L17
Clark, S. E., & Hensley, B. S. 2019, ApJ, 887, 136
Colombo, D., Meidt, S. E., Schinnerer, E., et al. 2014, ApJ, 784, 4
Crosthwaite, L. P., Turner, J. L., Buchholz, L., Ho, P. T. P., & Martin, R. N. 2002, AJ, 123, 1892
Daigle, O., Carignan, C., Amram, P., et al. 2006, MNRAS, 367, 469
Dapp, W. B., & Basu, S. 2010, A&A, 521, L56
Dicaire, I., Carignan, C., Amram, P., et al. 2008, MNRAS, 385, 553
Dobbs, C., & Baba, J. 2014, PASA, 31, e035
Dowell, C. D., Cook, B. T., Harper, D. A., et al. 2010, Proc. SPIE, 7735, 77356H
Elmouttie, M., Haynes, R. F., Jones, K. L., Sadler, E. M., & Ehle, M. 1998a, MNRAS, 297, 1202
Elmouttie, M., Krause, M., Haynes, R. F., & Jones, K. L. 1998b, MNRAS, 300, 1119
Elvius, A. 1972, A&A, 19, 193
Elvius, A. 1978, A&A, 65, 233
Erwin, P. 2005, MNRAS, 364, 283
Evirgen, C. C., Gent, F. A., Shukurov, A., Fletcher, A., & Bushby, P. 2017, MNRAS, 464, L105
Federrath, C. 2016, NewA, 82, 535820601
Ferrarese, L., Mould, J. R., Stetson, P. B., et al. 2007, ApJ, 654, 186
Fletcher, A., Beck, R., Shukurov, A., Berkhuijsen, E. M., & Horellou, C. 2011, MNRAS, 412, 2396
Font, J., Beckman, J. E., James, P. A., & Patsis, P. A. 2019, MNRAS, 482, 5362
Frick, P., Stepanov, R., Beck, R., et al. 2016, A&A, 585, A21
Gent, F. A. 2012, PhD thesis, Newcastle Univ.

Gressel, O., Elstner, D., Ziegler, U., & Rüdiger, G. 2008a, A&A, 486, L35
Gressel, O., Ziegler, U., Elstner, D., & Rüdiger, G. 2008b, Frontiers in Astronomy and Space Sciences, 329, 619
Harper, D. A., Runyan, M. C., Dowell, C. D., et al. 2018, JAI, 7, 1840008
Haverkorn, M., Brown, J. C., Gaensler, B. M., & McClure-Griffiths, N. M. 2008, ApJ, 680, 362
Heald, G., Braun, R., & Edmonds, R. 2009, A&A, 503, 409
Heesen, V., Beck, R., Krause, M., & Dettmar, R. J. 2011, A&A, 535, A79
Hsieh, P.-Y., Matsushita, S., Liu, G., et al. 2011, ApJ, 736, 129
Hummel, E., Lesch, H., Wielebinski, R., & Schlickeiser, R. 1988, A&A, 197, L29
Hunter, J. D. 2007, CSE, 9, 90
Izumi, T., Wada, K., Fukushige, R., Hamamura, S., & Kohno, K. 2018, ApJ, 867, 48
Jones, K. L., Koribalski, B. S., Elmouttie, M., & Haynes, R. F. 1999, MNRAS, 302, 649
Jones, T. J. 2000, AJ, 120, 2920
Jones, T. J., Dowell, C. D., Lopez Rodriguez, E., et al. 2019, ApJL, 870, L9
Jow, D. L., Hill, R., Scott, D., et al. 2018, MNRAS, 474, 1018
Karachentsev, I. D., Sharina, M. E., & Huchtmeier, W. K. 2000, A&A, 362, 544
Kennicutt, R. C. J., Armus, L., Bendo, G., et al. 2003, PASP, 115, 928
Kim, W.-T., & Stone, J. M. 2012, ApJ, 751, 124
Krasheninnikova, I., Shukurov, A., Ruzmaikin, A., & Sokolov, D. 1989, A&A, 213, 19
Krause, M., Irwin, J., Schmidt, P., et al. 2020, A&A, 639, A112
Kulsrud, R. M., & Zweibel, E. G. 2008, RPPh, 71, 046901
Kuno, N., Sato, N., Nakanishi, H., et al. 2007, PASJ, 59, 117
Lin, C. C., & Shu, F. H. 1964, ApJ, 140, 646
Lopez-Rodriguez, E. 2021, NatAs, 5, 604
Lopez-Rodriguez, E., Beck, R., Clark, S. E., et al. 2021a, ApJ, 923, 150
Lopez-Rodriguez, E., Borlaff, A. S., Beck, R., et al. 2023, ApJL, 942, L13
Lopez-Rodriguez, E., Clarke, M., Shenoy, S., et al. 2022a, ApJ, 936, 65
Lopez-Rodriguez, E., Dowell, C. D., Jones, T. J., et al. 2020, ApJ, 888, 66
Lopez-Rodriguez, E., Guerra, J. A., Asgari-Targhi, M., & Schmelz, J. T. 2021b, ApJ, 914, 24
Lopez-Rodriguez, E., Mao, S. A., Beck, R., et al. 2022b, ApJ, 936, 92
Lou, Y.-Q., & Fan, Z. 1998, ApJ, 493, 102
Lucero, D. M., Carignan, C., Elson, E. C., et al. 2015, MNRAS, 450, 3935
Maiolino, R., Alonso-Herrero, A., Anders, S., et al. 2000, ApJ, 531, 219
Mardia, K. V. 1972, Statistics of Directional Data, Probability and Mathematical Statistics: A Series of Monographs and Textbooks (London: Academic Press), ibc1
Martin-Alvarez, S., Devriendt, J., Slyz, A., et al. 2022, MNRAS, 513, 3326
Martin-Alvarez, S., Slyz, A., Devriendt, J., & Gómez-Guijarro, C. 2020, MNRAS, 495, 4475
Martini, P., Regan, M. W., Mulchaey, J. S., & Pogge, R. W. 2003, ApJS, 146, 353
Mayya, Y. D., Carrasco, L., & Luna, A. 2005, ApJL, 628, L33
McQuinn, K. B. W., Skillman, E. D., Dolphin, A. E., Berg, D., & Kennicutt, R. 2017, AJ, 154, 51
Mestel, L., & Subramanian, K. 1991, MNRAS, 248, 677
Mouschovias, T. C., & Ciolek, G. E. 1999, in The Origin of Stars and Planetary Systems, ed. C. J. Lada & N. D. Kylafis, Vol. 540 (Dordrecht: Kluwer), 305
Ntormousi, E., Tassis, K., Del Sordo, F., Fragkoudi, F., & Pakmor, R. 2020, A&A, 641, A165
Patrikeev, I., Fletcher, A., Stepanov, R., et al. 2006, A&A, 458, 441
Pattle, K., Fissel, L., Tahani, M., Liu, T., & Ntormousi, E. 2022, arXiv:2203.11179
Pavel, M. D., & Clemens, D. P. 2012, ApJL, 761, L28
Pillai, T. G. S., Clemens, D. P., Reissl, S., et al. 2020, NatAs, 4, 1195
Planck Collaboration, Adam, R., Ade, P. A. R., et al. 2016, A&A, 586, A135
Planck Collaboration, Ade, P. A. R., Aghanim, N., et al. 2015, A&A, 576, A104
Quillen, A. C., Neumayer, N., Oosterloo, T., & Espada, D. 2010, PASA, 27, 396
Radburn-Smith, D. J., de Jong, R. S., Seth, A. C., et al. 2011, ApJS, 195, 18
Rees, M. J. 1987, QJRAS, 28, 197
Rincon, F. 2019, NewA, 85, 205850401
Robitaille, T., & Bressert, E. 2012, APLpy: Astronomical Plotting Library in Python, Astrophysics Source Code Library, ascl:1208.017
Roussel, H., Wilson, C. D., Vigroux, L., et al. 2010, A&A, 518, L66
Ruiz-Granados, B., Rubiño-Martín, J. A., Florido, E., & Battaner, E. 2010, ApJL, 723, L44
Ruzmaikin, A., Sokolov, D., & Shukurov, A. 1988, Natur, 336, 341

Scarrott, S. M., Draper, P. W., Stockdale, D. P., & Wolstencroft, R. D. 1993, MNRAS, 264, L7

Scarrott, S. M., Rolph, C. D., Wolstencroft, R. W., & Tadhunter, C. N. 1991, MNRAS, 249, 16P

Sellwood, J. A. 2011, MNRAS, 410, 1637

Serkowski, K. 1974, MExP, 12, 361

Seta, A., & Federrath, C. 2022, MNRAS, 514, 957

Shukurov, A. 1998, MNRAS, 299, L21

Soida, M., Urbanik, M., Beck, R., Wielebinski, R., & Balkowski, C. 2001, A&A, 378, 40

Sokoloff, D. D., Bykov, A. A., Shukurov, A., et al. 1998, MNRAS, 299, 189

Subramanian, K. 2016, RPPh, 79, 076901

Surgent, W. J., Lopez-Rodriguez, E., & Clark, S. E. 2023, arXiv:2302.07278

Tahani, M., Glover, J., Lupypciw, W., et al. 2022a, A&A, 660, L7

Tahani, M., Lupypciw, W., Glover, J., et al. 2022b, A&A, 660, A97

Tarchi, A., Greve, A., Peck, A. B., et al. 2004, MNRAS, 351, 339

Tully, R. B. 1988, Nearby Galaxies Catalog (Cambridge: Cambridge Univ. Press)

Tully, R. B., Courtois, H. M., Dolphin, A. E., et al. 2013, AJ, 146, 86

Tully, R. B., Rizzi, L., Shaya, E. J., et al. 2009, AJ, 138, 323

Vacca, W. D., Hamilton, R. T., Savage, M., et al. 2015, ApJ, 804, 66

Vaillancourt, J. E., Chuss, D. T., Crutcher, R. M., et al. 2007, Proc. SPIE, 6678, 66780D

van de Voort, F., Bieri, R., Pakmor, R., et al. 2021, MNRAS, 501, 4888

Verstappen, J., Fritz, J., Baes, M., et al. 2013, A&A, 556, A54

Widrow, L. M. 2002, RvMP, 74, 775

Wiegert, T., Irwin, J., Miskolczi, A., et al. 2015, AJ, 150, 81

Willick, J. A., Courteau, S., Faber, S. M., et al. 1997, ApJS, 109, 333

Zschaechner, L. K., Walter, F., Bolatto, A., et al. 2016, ApJ, 832, 142